

Crystal Phase Control in Two-Dimensional Materials

Jialiang Wang¹, Yang Wei¹, Hai Li^{1*}, Xiao Huang^{1*} & Hua Zhang^{2*}

¹ Institute of Advanced Materials (IAM), Nanjing Tech University (NanjingTech), 30 South Puzhu Road, Nanjing 211816, P.R. China

² Center for Programmable Materials, School of Materials Science and Engineering, Nanyang Technological University, 50 Nanyang Avenue, Singapore 639798, Singapore

Received ***, accepted ***, published online ***

It is the nature of crystals to exist in different polymorphs. The recent emergence of two-dimensional (2D) materials has evoked the discovery of a number of new crystal phases that are different from their bulk structures at ambient conditions, and revealed novel structure-dependent properties, which deserve in-depth understanding and further exploration. In this contribution, we review the recent development of crystal phase control in 2D materials, including group VI transition metal dichalcogenides (TMDs), group IVA metal chalcogenides and noble metals. For each group of materials, we begin with introducing the various existing crystal phases and their structure-related properties, followed by a detailed discussion on factors that influence these crystal structures and thus the possible strategies for phase control. Finally, after summarizing the whole paper, we present the challenges and opportunities in this research direction.

Crystal phase control, metal chalcogenides, noble metals, two-dimensional materials

1 Introduction

Two-dimensional (2D) materials, such as graphene [1-3] and transition metal dichalcogenides (TMDs), [4-8] have attracted great attention due to their novel properties and functions arising at the reduced dimensions, which may potentially lead to the advancement of future electronics, optoelectronics and energy-related systems. [9-11] Meanwhile, other inorganic 2D materials such as group IVA metal chalcogenides (IVAMCs) and noble metals have also received considerable attention due to their attractive electronic, optoelectronic, catalytic and electrocatalytic properties. [12-20]

A common feature of these materials lies in their tunable functional properties that closely correlate to not only their size, shape and composition, but also in particular, their crystal phases. [21, 22] A solid material existing in more than one crystalline structure, also termed as polymorphism, has been observed in TMDs (e.g. TiS_2 , MoS_2 , WTe_2 , TaSe_2 and NbS_2),

IVAMCs (e.g. SnS and SnS_2), III-V semiconducting compounds (e.g. GaAs and InAs) and noble metals (e.g. Ru , Au , Ag and Rh). [23] For example, group VI TMDs (VITMDs) nanosheets, such as MoS_2 and WS_2 , exist in either the hexagonal phase (2H) or the trigonal phase (1T), which exhibit the semiconducting or metallic properties, respectively. [4, 5] Some other TMDs, typically group IV (IVTMDs, e.g. TiS_2) and group V TMDs (VTMDs, e.g. TaS_2 , TaSe_2 , NbSe_2) have been also found to exhibit in 2H or 1T phase, exhibiting novel superconductivity (SC) or charge density wave (CDW) phases at low temperatures. [24, 25] Similarly, a number of phases including hexagonal, trigonal, orthorhombic and cubic structures have been identified in layered IVAMCs (e.g. SnS_2 and SnS), which show phase-dependent electronic band structure and dopant type. [14, 22, 26, 27] As for 2D noble metal nanostructures (e.g. Au and Rh), cubic, hexagonal and tetragonal crystal phases have been revealed, amongst which, those thermodynamically less favored phases show unusual optical properties and outstanding catalytic properties. [17, 19, 28, 29] Moreover, an artificial polymorph of graphene was achieved via a recently developed transfer technique,

*Corresponding authors (email: iamhli@njtech.edu.cn; iamxhuang@njtech.edu.cn; hzhang@ntu.edu.sg)

which exhibited unusual superconductivity.[30]

Because of the ultrathin nature of 2D materials, their structures are extremely sensitive to surface defects,[31, 32] chemical absorption [33, 34] and electric charges[35, 36]. Therefore, in addition to conventional strategies for phase transition such as thermal annealing [37, 38] and applying high pressure,[39, 40] other approaches such as ionic or atomic doping,[41-44] charging,[27, 45] and ligand exchange [29, 46] have been recently demonstrated to achieve effective crystal phase control in 2D materials.

In this contribution, we provide an overview of representative strategies for the crystal phase control of the aforementioned 2D nanomaterials, including TMDs, IVAMCs and 2D noble metals.

2 Transition Metal Dichalcogenides (TMDs)

Over the past years, single- to few-layer TMDs have demonstrated a number of interesting and important features, such as tunable band gaps,[9, 37, 47] strong spin-orbit coupling,[48-50] high catalytic/electrocatalytic activities, [51-53] and good mechanical strength,[54-56] which make them appealing for both fundamental studies and practical applications.[4-8]

TMDs have a general chemical formula of MX_2 , where M is a transition metal (such as Ti, V, Nb, Mo, Hf, Ta and W) and X stands for S, Se or Te. Each layer exhibits a “sandwich” type of structure (X-M-X) in which the transition metal (M) is covalently bonded with two chalcogens (X).[5] Adjacent layers are further bound by weak van der Waals forces which can be feasibly overcome to enable the exfoliation and isolation of single- to few-layered nanosheets.[57] TMDs exist in several structural polytypes (Figure 1), typically involving the trigonal prismatic (1H) or octahedral (1T) coordination.[5, 58] With the varied stacking sequence of 1H layers, the hexagonal 2H (i.e. 2H_a and 2H_b) and rhombohedral 3R

phases can be achieved, which include two and three X-M-X primary 1H layers, respectively (Figure 1b-d). Besides, two kinds of distorted 1T phase, namely the $1\text{T}'$ and T_d phase, have also been observed, exhibiting the monoclinic (space group $\text{P}2_1/m$) (Figure 1f) and orthorhombic (space group $\text{Pnm}2_1$) (Figure 1g) structures. The thermodynamically stable structure for most VITMDs is usually in the 2H_b phase, whereas VTMDs are inclined to the 2H_a phase.[58] An exception is WTe_2 , whose stable bulk phase at room temperature is the orthorhombic T_d phase.[59, 60]

TMDs exhibit diverse kinds of electronic characters, including metallic, semimetallic, semiconducting and superconducting behavior, which are highly dependent on their crystal phases. For most VITMDs, while the 2H-phased structures are semiconducting, the $1\text{T}(1\text{T}', \text{T}_d)$ -phased ones are metal-like.[4, 5, 35, 60-62] Importantly, the semiconducting-phased nanosheets such as MoS_2 have shown large on/off ratios and high carrier mobilities for field effect transistors (FETs),[63, 64] whereas the metallic counterparts have been recently found to be highly active towards the hydrogen evolution reaction (HER)[51-53, 65]. Moreover, low resistance contacts have been realized by creating $1\text{T}(1\text{T}')$ -2H (metal-semiconductor) phase-heterostructures.[66, 67] In addition, the phase-dependent CDW phases at low temperatures have been demonstrated in VTMDs, including TaS_2 , TaSe_2 , and NbSe_2 . [24] Very recently, an unprecedented polymorph of TaS_2 with an increased CDW transition temperature was revealed by exfoliating a bulk 2H_a TaS_2 crystal into ultrathin flakes.[68] Therefore, reliable strategies that can realize phase transition on a large scale are of particular scientific and practical interest.

To date, many methods have been developed to realize crystal-phase controlled preparation of TMDs. In this section, strategies including ion intercalation,[41, 42, 53, 69-72] charging,[45] alloying/doping,[43, 44, 73] defect engineering,[32, 66, 74, 75] strain engineering,[40, 61, 76, 77] electrostatic gating,[35, 36] and thermal activation[37, 38, 78] will be discussed.

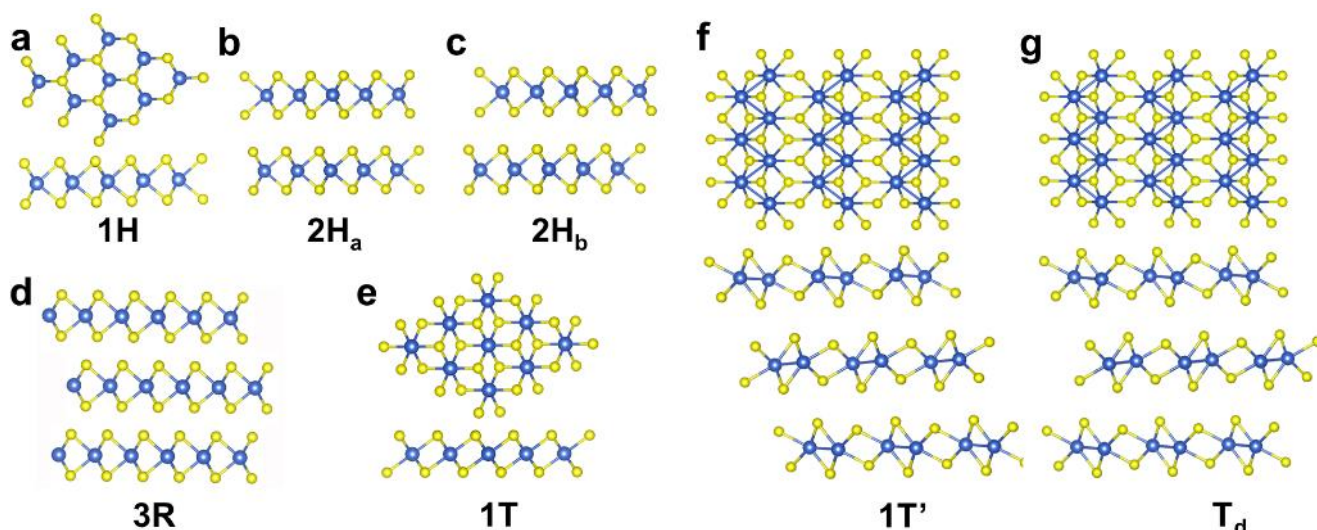


Figure 1 Structural models of transition metal dichalcogenides (TMDs) in their (a) 1H, (b) 2H_a, (c) 2H_b (d) 3R, (e) 1T, (f) 1T' and (g) T_d phases, where blue spheres represent metals and yellow spheres represent chalcogens. In (a,e,f,g), the top part shows the planar view of a single layer, and the bottom part shows the side view of single or few stacked layers. (b,c,d) Side view of stacked layers.

2.1 Ion intercalation

TMDs together with other layered materials were found to be chemically intercalatable with a number of alkali metal reagents, such as *n*-butyllithium and metal naphthalenide (metal = Li, Na and K).[79-82] Intercalation of cations can expand the gap between adjacent TMD layers and thus weaken the van der Waals interaction to enable their isolation via subsequent agitation. The Li-intercalated compounds can also be obtained with our previously developed electrochemical lithiation method, which can be implemented at milder conditions compared to the chemical intercalation method.[41, 69] As shown in Figure 2a, TMD bulk crystals are typically coated on a metal foil (e.g. Cu) and assembled in a Li ion battery cell as the cathode, and a piece of Li foil used as the anode. After discharging, the obtained Li_xMX₂ compounds are immersed and sonicated in water/ethanol to obtain the exfoliated TMD nanosheets.

For both chemical and electrochemical lithium intercalation, the original 2H TMDs have been found to partially transform to the 1T and distorted 1T' phase.[52, 67, 83] Structural changes in these intercalated compounds in fact have been observed since as early as 1980s.[84-87] With the advancing of electron microscopy techniques, microstructures of these crystal phases can be studied more directly. For example, Eda and co-workers prepared crystal phase heterostructures of MoS₂ via Li-intercalation.[83] Under the Cs-corrected scanning transmission electron microscopy (STEM) imaging, three phases were identified, including the 2H, 1T and 1T' phase consisting of zig-zag chains (Figure 2b-d). The

mechanism behind the 2H-to-1T(1T') phase transition was then investigated theoretically by several groups.[88-91] In the case of MoS₂ and WS₂, electrons transferred from the alkali metals (e.g. Li, Na, K etc.) during intercalation could cause an increase in the electron density of the d-orbital of the transition metal, inducing the destabilization of the pristine 2H phase and its transition to the metallic 1T or distorted 1T' phase.[92-94]

As an alternative to the post-growth intercalation-induced phase transition, Yu et al. recently reported the direct preparation of micrometer-sized 1T'-MoX₂ (X = S, Se) (Figure 2e-f) via the sulfurization of potassium molybdate (KMoO₄). [72] The high purity 1T'-phase was confirmed by STEM, X-ray diffraction (XRD), and X-ray photoelectron spectroscopy (XPS) analyses (Figure 2g-h). The formation and stabilization of the 1T' phase can be attributed to the presence of potassium counterions that may increase the electron density of Mo.

Since electron doping is the main cause to the formation of the 1T(1T') phase, doping agents other than alkali metals such as ammonium containing precursors [42, 70] and hydrazine hydrate [71] have also been used for the in-situ preparation of 1T (1T') TMDs. For example, Liu et al. reported the synthesis of 1T (1T') phased WS₂ ultrathin nanoribbons (N-WS₂) via a direct hydrothermal reaction between (NH₄)₁₀W₁₂O₄₁·xH₂O and thiourea.[42] In combine with theoretical calculations, they suggested that about 0.75 electrons per NH₄ were transferred to WS₂, resulting in the formation of WS₂⁻·NH₄⁺ ionic complex. With a similar approach, we recently directly synthesized alloyed Mo_{1-x}W_xS₂ nanosheets with tunable 1T(1T')/2H phase ratios.[70]

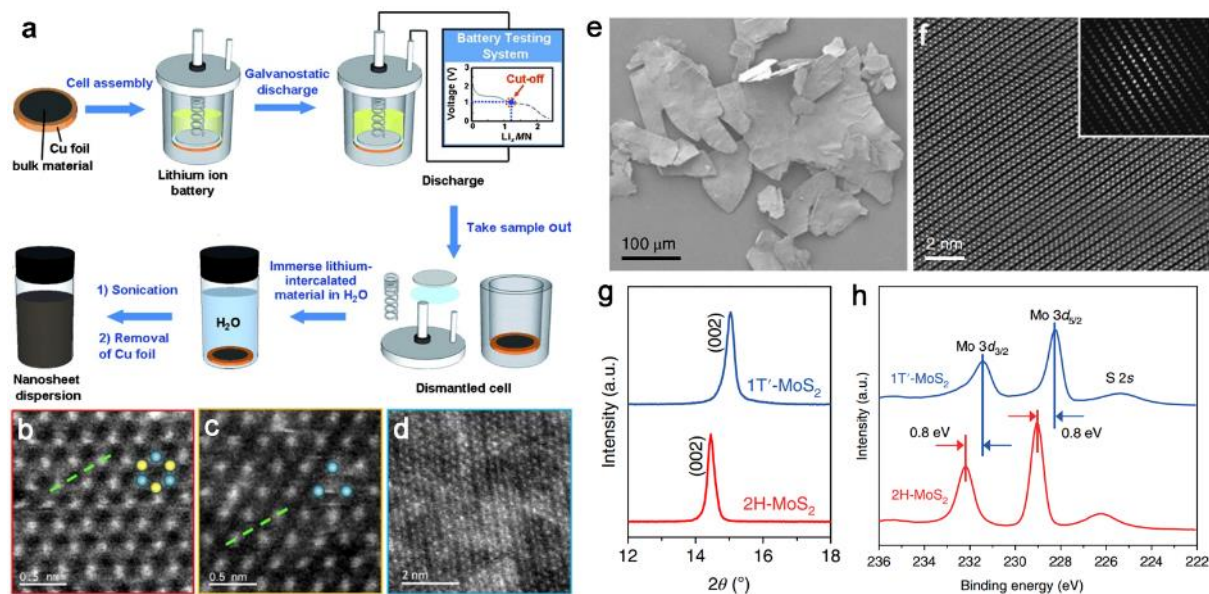


Figure 2 (a) Scheme of the electrochemical lithium intercalation process to produce 2D nanosheets from the layered bulk material. Reproduced with permission from ref. [41]. Copyright 2012, John Wiley & Sons, Inc. (b-d) High resolution STEM images of (b) 2H, (c) 1T, and (d) 1T' phases. The blue and yellow balls in image b and c indicate the position of Mo and S atoms. Reproduced with permission from ref. [83]. Copyright 2012, American Chemical Society. (e) Scanning electron microscopy (SEM) image of the prepared 1T'-MoS₂ crystals. (f) STEM image of a single-layer 1T'-MoS₂ nanosheet. The asymmetric distribution of atoms is clearly shown. Inset: corresponding FFT diffraction. (g) Magnified XRD patterns of the (002) peaks of 1T' and 2H-MoS₂ crystals, from the red dashed area in g. (h) XPS Mo 3d spectra of 1T'-MoS₂ crystals and 2H-MoS₂ crystals obtained by annealing 1T'-MoS₂ crystals. Reproduced with permission from ref. [72]. Copyright 2018, Nature Publishing Group.

2.2 Alloying/doping

Considering the composition-dependence of crystal phases, alloying between TMDs with dissimilar crystal structures is expected to realize phase transitions.[44, 73] Due to the fact that WTe₂ is a special case in VITMDs that its thermodynamic stable structure is the T_d phase[60], WTe₂ has been chosen to study the alloying induced phase transitions. For instance, Rhodes et al. prepared Mo_{1-x}W_xTe₂ alloys with chemical vapor transport (CVT) method and created a simplified phase diagram for the alloying system.[44] It can be seen that the semimetallic orthorhombic phase (T_d) is preferred over the 2H phase for W concentrations (x_c) larger than 0.08 (Figure 3a-e). Similarly, Yu et al. reported the CVT growth of WSe_{2(1-x)}Te_{2x} (x = 0-1) and observed a gradual transition from the 2H to T_d structure with increasing x value, specifically, x = 0-0.4 for 2H structure, x = 0.5 and 0.6 for mixed 2H and T_d structures, and x = 0.7-1.0 for T_d structure (Figure 3f).[73]

As for VTMDs, Luo et al. reported the synthesis of TaSe_{2-x}Te_x (0 ≤ x ≤ 2) crystals with 2H, 3R, 1T, and monoclinic phases (Figure 3g).[95] They found that only a small concentration of Te doping (x = 0.02) could lead to 2H-to-3R transition. Interestingly, at 0.1 ≤ x ≤ 0.35, the 3R-TaSe_{2-x}Te_x showed the coexistence of superconductivity and a CDW phase at above 0.4 K. At higher Te substitutions (1.8 ≤ x ≤ 2), TaSe_{2-x}Te_x becomes the metallic monoclinic polymorph.

Apart from alloying, doping with elements from different groups with larger atomic disparity could also cause the

phase transitions in TMDs.[43, 88] Some previous reports showed that MoS₂ would take the 3R phase when minority Mo atoms were substituted by elements like Re or Nb.[96] Besides the 2H-to-3R phase transition, a recent study showed that substitutional Re doping in 2H-phased WS₂ nanotubes could induce their partial transformation to the 1T phase.[88] More recently, Kochat et al. [43] reported the chemical vapor deposition (CVD) growth of Re-doped MoSe₂ and found that increasing Re concentration stabilized the 1T' phase. This was further supported by DFT calculations that substitution of each Mo with a Re could lead to the addition of an extra electron which destabilized the 2H phase to transform to the 1T' phase.

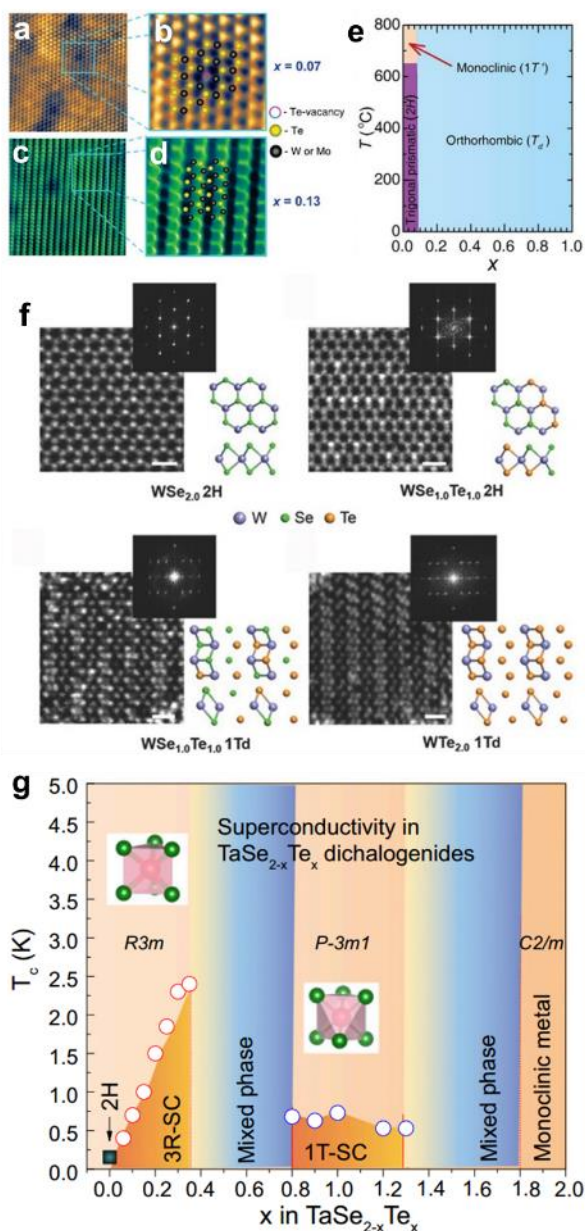


Figure 3 (a) Scanning tunneling microscopy (STM) image of a $\text{Mo}_{1-x}\text{W}_x\text{Te}_2$ single crystal with $x = 0.07$, showing a clear hexagonal pattern as expected for the 2H-phase. (b) Magnification of a local area where one can detect a Te vacancy. (c) STM image of a $\text{Mo}_{1-x}\text{W}_x\text{Te}_2$ single crystal with $x = 0.13$, showing a pattern of parallel chains as expected for the orthorhombic phase. (d) Magnification of a local region revealing the intrachain structure and illustrating the crystallographic positions of transition metal (black dots) and Te (yellow dots) atoms, respectively. (e) Bulk phase-diagram of the $\text{Mo}_{1-x}\text{W}_x\text{Te}_2$ series based on the array of experimental techniques. Reproduced with permission from ref. [44]. Copyright 2016, John Wiley & Sons, Inc. (f) Atomic resolution STEM characterization of $\text{WSe}_{2(1-x)}\text{Te}_{2x}$ ($x = 0-1$) alloyed monolayers with different Te concentration. Reproduced with permission from ref. [73]. Copyright 2017, John Wiley & Sons, Inc. (g) The composition stability ranges of the 2H, 3R, 1T, and monoclinic MX_2 forms in $\text{TaSe}_{2-x}\text{Te}_x$ and the dependence of T_c on x . The TaX_2 coordination polyhedra are highlighted. Single-phase regions are shown in pink, and multiple-phase regions are shown in blue. Reproduced with permission from ref. [95]. Copyright 2015, National Academy of Sciences of the United States of America.

2.3 Defect engineering

Defects in TMDs, typically metal and chalcogen vacancies, can induce profound modification of their chemical, structural and electronic properties.[31, 32, 66, 74] As a typical example of defect engineering-assisted phase control, Zhou et al. [75] found that Te vacancies were created during the growth of MoTe_2 when insufficient Te source was provided to react with MoO_3 . [66] This led to the formation of 1T' MoTe_2 instead of 2H MoTe_2 (Figure 4a).

Alternatively, post-growth defect engineering can be implemented to control the phase of TMDs. Up to date, several high-energy sources including electron-beam,[74] laser [66] and Ar plasma [32] have been used to generate local structural distortions or atomic defects in TMDs. For example, Cho et al. realized a heterophase homojunction between semiconducting 2H and metallic 1T' phase by using laser irradiation to form an ohmic contact in the MoTe_2 transistor (Figure 4b-f). [66] Theoretical calculations revealed that the phase transition might originate from the Te vacancies at an elevated temperature, and the 1T' phase became more stable than the 2H phase when the Te monovacancy concentration was above 3% (Figure 4g).

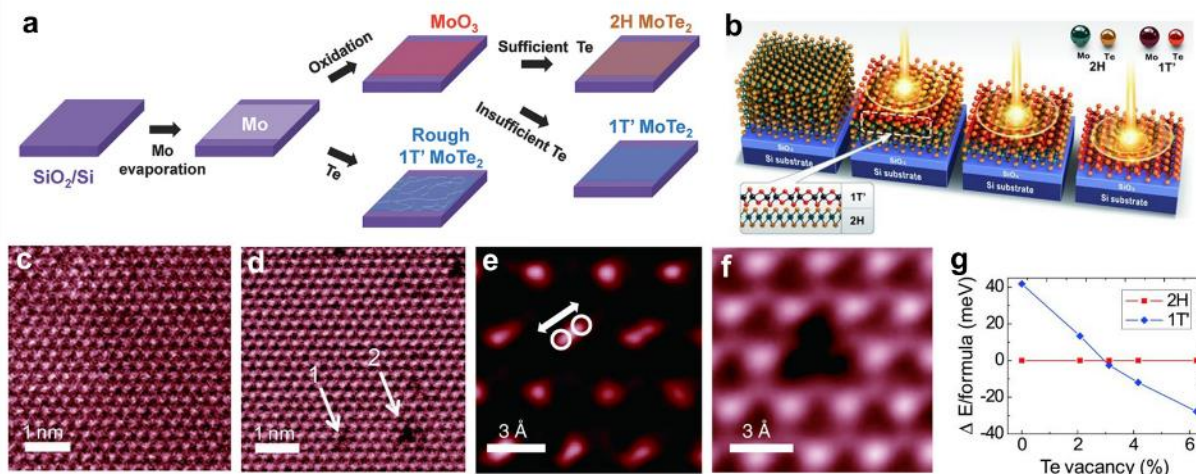


Figure 4 (a) A schematic illustration of the growth process for $1\text{T}'$ and 2H MoTe_2 using Mo and MoO_3 as precursors. Reproduced with permission from ref. [75]. Copyright 2016, John Wiley & Sons, Inc. (b) Schematic representation of the laser-irradiation process. (c) Atomic image of a monolayer of 2H-MoTe_2 . Bright spheres are Te atoms with hexagonal symmetry. (d) Atomic Te vacancies created artificially. Te single vacancy and divacancy are visible and marked by 1 and 2, respectively. (e) Filtered high-resolution image near a Te vacancy showing the splitting of the Te atoms. (f) Atomic resolution image of a Te divacancy defect. (g) The energy differences between the 2H and $1\text{T}'$ phases as a function of the Te vacancy concentration from the DFT calculation. Reproduced with permission from ref. [66]. Copyright 2015, American Association for the Advancement of Science.

2.4 Strain engineering

Crystal lattices under strain can be contracted or dilated, leading to the change of relative atomic positions and thus the modification of crystal phases. Duerloo et al. theoretically demonstrated the possibility of using mechanical deformation to thermodynamically induce phase transition of VITMDs.[61] It was shown that for most VITMDs, equibiaxial tensile strains of 10–15% were required to achieve the transition from the semiconducting to the metallic phase.[61, 97] As an exception, MoTe_2 can be transformed under a minimal tensile strain of only 0.3–3% at room temperature. This is likely due to the fact that the energy difference between 2H- and $1\text{T}'\text{-MoTe}_2$ was approximately only 40 meV based on first-principles calculations, which was much smaller than that of other TMDs.[61]

Experimentally, strain has been created in TMDs based on the lattice mismatch between epitaxial films and substrates, by bending of films on flexible substrates, and by applying pressure with an atomic force microscope (AFM) tip or a diamond anvil cell (DAC).[40, 61, 76, 77] For instance, Nayak et al. investigated the effect of pressure on the electronic, vibrational, optical and structural properties of multilayered MoS_2 , and found that the multilayered 2H MoS_2 transformed to an intermediate state (IS) at ~ 10 GPa and then to the metallic phase at > 19 GPa (Figure 5a-b).[40] First-principle calculations suggested that the high pressure could cause a reduction in the interlayer spacing and an enhanced S–S interaction, which led to the overlap of the valence and conduction bands (Figure 5c-d).

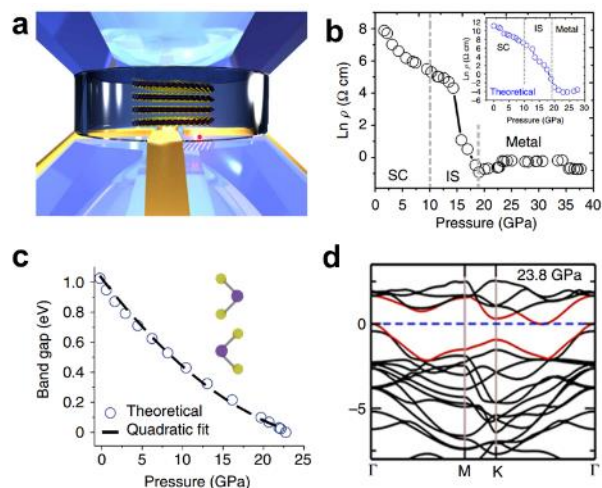


Figure 5 (a) A 3D illustration of multilayered MoS_2 in a DAC pressure medium for compression experiments. (b) Pressure-dependent electrical resistivity of MoS_2 . Three characteristic regions have been identified: semiconducting (SC), intermediate state (IS) and metallic regions. Inset: theoretically calculated pressure-dependent electrical resistivity. (c) Theoretical calculation of the pressure-dependent band gap of multilayered MoS_2 . (d) Theoretical band structure of multilayered MoS_2 under hydrostatic pressure of 23.8 GPa. VBM and CBM are shown by red lines. Reproduced with permission from ref. [40]. Copyright 2014, Nature Publishing Group.

2.5 Electrostatic gating

Li et al. pointed out based on DFT calculations, that the reversible $2\text{H-to-}1\text{T}'$ phase transition in monolayer TMDs, including MoTe_2 , MoS_2 and TaSe_2 , could be induced by electrostatic gating through change of carrier density and electron chemical potential.[35] This was later realized experimentally by Wang et al., who demonstrated the $2\text{H-to-}1\text{T}'$ phase transition in monolayer MoTe_2 placed as the

channel in an ionic liquid-gated field effect transistor (FET) (Figure 6a-d).[36] Reversible phase transition was demonstrated by increasing or decreasing the gate voltage (Figure 6c). Markedly, such phase transition occurred simultaneously across the whole MoTe_2 monolayer and the crystal orientation was perfectly preserved (Figure 6d).

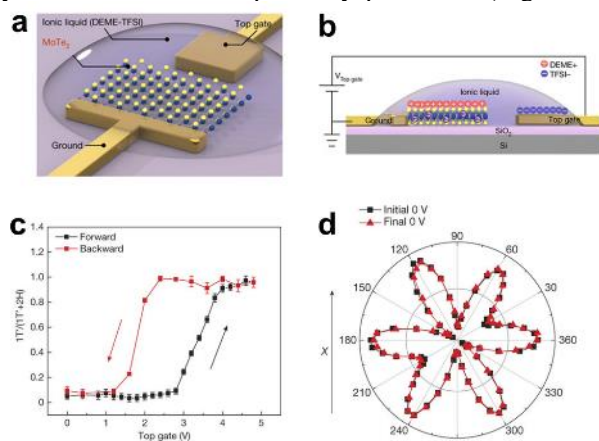


Figure 6 (a, b) Schematics and measurement configuration of a MoTe_2 monolayer field-effect transistor. (c) Gate-dependent Raman intensity ratios. The ratio $F = I_{1T}(A_g)/[2I_{2H}(A_1') + I_{1T}(A_g)]$ (y-axis) shows hysteresis under an electrical field scan, with a loop width as large as 1.8 V. The black and red curves show increasing and decreasing gate voltage, respectively. (d) SHG intensity from the same monolayer sample as a function of crystal angle. The initial 2H phase at 0 V shows a typical sixfold pattern (black squares connected by a black line). Reproduced with permission from ref. [36]. Copyright 2017, Nature Publishing Group.

2.6 Stability of metastable phases

In the above sections, a number of growth and post-growth methods have been employed to obtain metastable phases of TMDs. When sufficient energy is provided, these metastable structures would be converted back to their thermodynamic stable structures, such as through thermal annealing [37, 62]

and infrared (IR) laser-induced heating.[38, 78] For example, the thermally driven transformation of 1T/1T' MoS_2 back to the 2H phase was studied using in situ Raman spectroscopy by Guo et al.[78] An activation energy of 400 ± 60 meV (38 ± 6 kJ/mol) was calculated for the phase transition based on the temperature dependence of the transformation rate fitted to an Arrhenius expression. Importantly, this analysis revealed that the 1T/1T' phased MoS_2 has a half-life of about 10 days at room temperature and about only 5 h at 400 K.

Surface functionalization of TMDs in metastable phases has recently been demonstrated to improve their stability.[33, 34] For example, Voiry et al. used organic halides or I_2 to covalently or non-covalently functionalize the electron-rich metallic 1T TMDs, respectively, both leading to the quenching of their negative charges and thus the improved stability (Figure 7a).[33] In addition, it is worth noting that after functionalization, while the lattice structure of the 1T phase remained unchanged, its electronic property is remarkably altered from metallic to semiconducting, giving rise to a strong and tunable photoluminescence (Figure 7b-c).

Unfortunately, the improved stability is usually at the expense of surface chemical/electrochemical activities. Very recently, Benson et al. systematically investigated the correlation between the electron donating strength of the surface ligands and the surface energetics, electron transfer resistance, and the HER catalytic activity of thus-functionalized 1T- MoS_2 nanosheets (Figure 7d-e).[34] They found that although 1T- MoS_2 could be substantially stabilized by covalent surface functionalization, its HER catalytic activity was greatly suppressed due to appreciable reduction in its electron density. More evidently, the loss of HER activity became severer when the 1T- MoS_2 was functionalized by ligands with higher electron withdrawing ability.

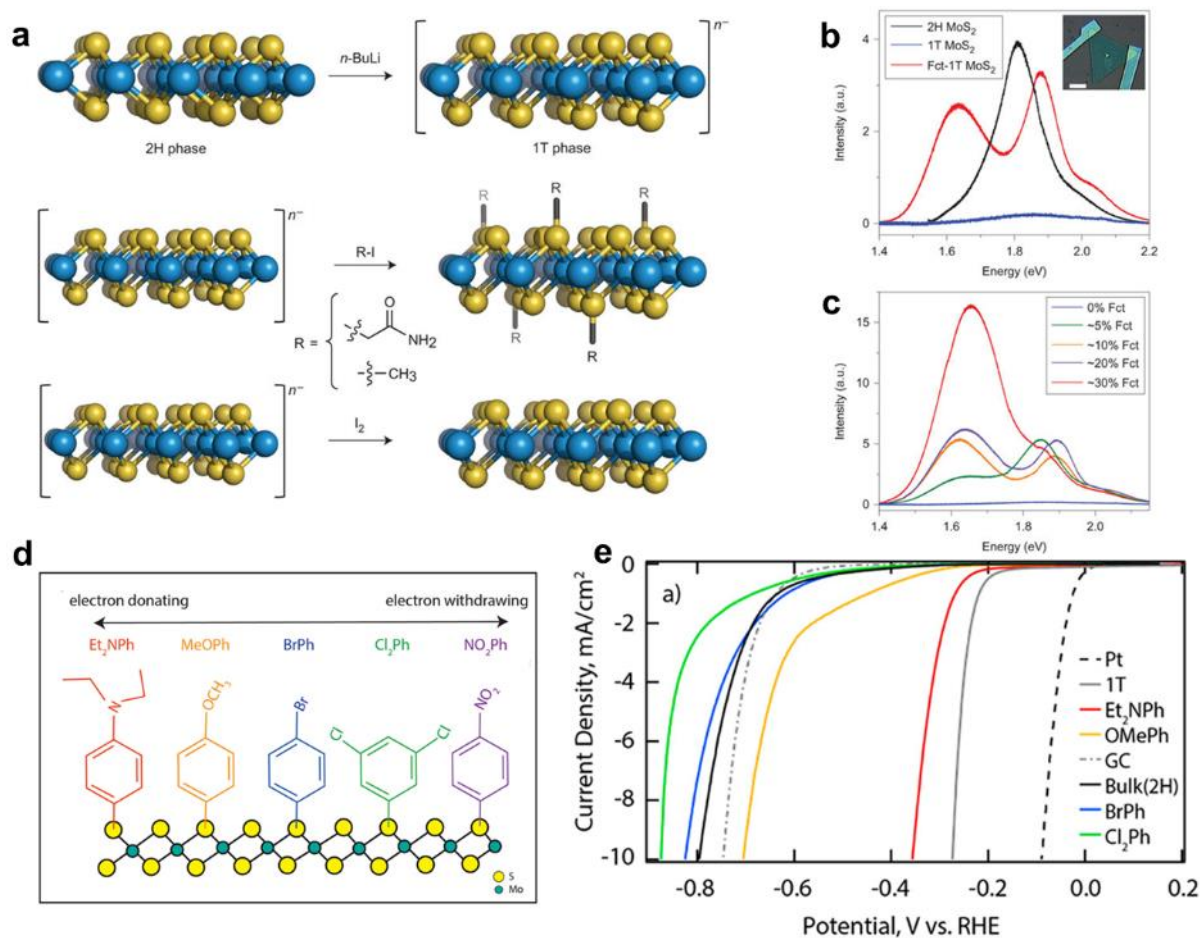


Figure 7 (a) Schematic of functionalization scheme. (Row 1) The 2H phase of TMDs is converted to the 1T phase via lithiation using butyllithium (BuLi), and the 1T phase is negatively charged. n^- indicates the excess charges carried by the exfoliated 1T-phase nanosheets. (Row 2) The nanosheets are functionalized using 2-iodoacetamide or iodomethane (R-I) solution. (Row 3) The charge on the nanosheets can also be quenched by reacting with iodine, with no covalent functionalization. (b) Photoluminescence spectra obtained from single-layer MoS₂ grown by CVD (2H phase), from the metallic 1T phase and from the functionalized 1T phase. (c) Modulation of photoluminescence peak intensity with increasing amount of functionalization: blue, 0% Fct; green, ~5% Fct; orange, ~10% Fct; purple, ~20% Fct; red, ~30% Fct. Photoluminescence peaks are normalized to the Raman peak of silicon at 520 cm⁻¹. Reproduced with permission from ref. [33]. Copyright 2014, Nature Publishing Group. (d) Schematic of the various functional groups on 1T MoS₂. (e) Linear sweep voltammograms (LSV) for glassy carbon electrodes deposited with functionalized, 1T, and bulk (2H) MoS₂. Reproduced with permission from ref. [34]. Copyright 2018, American Chemical Society.

3 Layered group-IVA metal chalcogenides

As an important sub-group of 2D layered materials, group-IVA metal chalcogenides (IVAMCs, metal = Ge, Sn; chalcogen = S, Se, Te) have aroused intensive research interest due to their attractive electronic and optoelectronic properties, combined with earth abundancy, low cost, and environmental friendliness.[12-16]

According to the metal/chalcogen stoichiometric ratio, IVAMCs take either the formula of MX (e.g. GeS, GeSe, SnS, SnSe, SnTe,) or MX₂ (e.g. GeS₂, GeSe₂, SnS₂, SnSe₂).[22]

Hexagonal, trigonal, orthorhombic and monoclinic crystal structures have been identified in IVAMCs.[27, 98-102] Taking SnS as an example, it exists in two polymorphous crystal phases, namely orthorhombic (space group Pnma) and cubic phase (space group Cmcm) (Figure 8).[101] Differently, SnS₂ can crystallize into the trigonal or hexagonal structure in which one monolayer of Sn atoms are sandwiched by two layers of S atoms, and similar to TMDs, depending on the type of Sn-S coordination as well as the stacking sequence of the adjacent S-Sn-S layers, 1T, 2H, and 4H polytypes of SnS₂ have been reported.[26, 27, 98, 99]

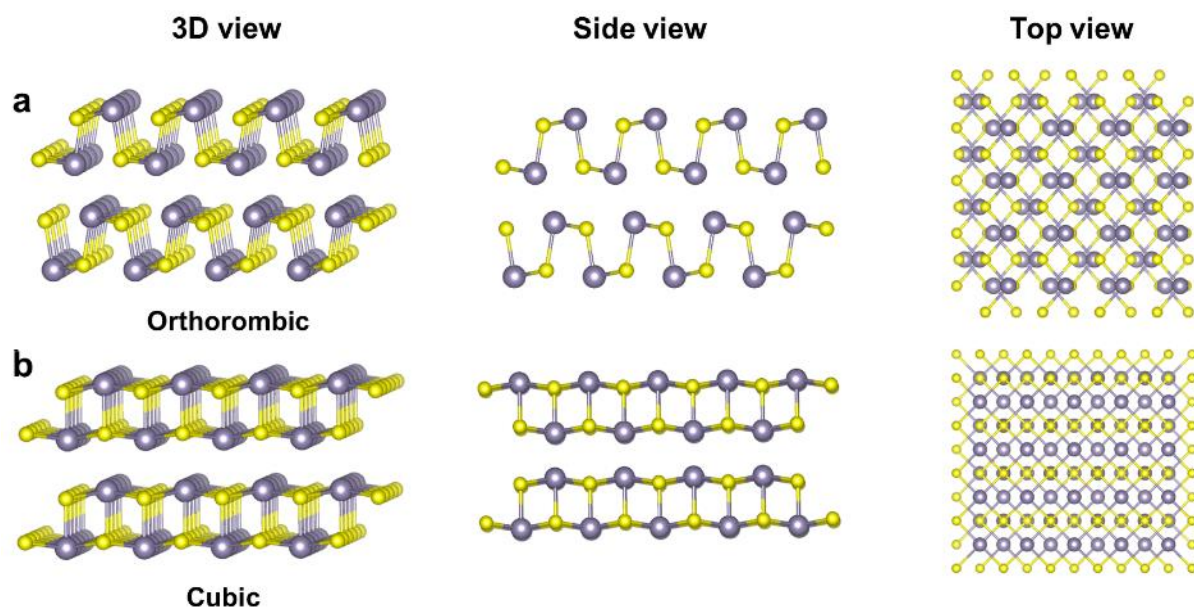


Figure 8 Structural models of layered orthorhombic (a) and cubic (b) phased IVAMCs. The left, middle and right columns show the 3D-view, side view and top planar view, respectively.

Although unlike TMDs, IVAMCs are semiconductors regardless of their phases, their semiconducting properties, in terms of bandgaps and dopant type, vary distinctively with crystal phases.[12-15, 26, 27, 103-108] For example, SnS is a p-type semiconductor with narrow direct and indirect bandgaps of 1.3 and 1.07 eV, respectively, resulting in a high absorption coefficient in the near-infrared spectral range for photodetectors, solar cells, photothermal therapy and so on.[103, 104] Importantly, its puckered in-plane structure gives rise to highly anisotropic optical and electronic properties.[105, 106] In sharp contrast, SnS₂ is an n-type semiconductor and possesses a symmetric in-plane structure and thus isotropic optical properties with an indirect bandgap of ~2.2-2.7 eV.[26, 27] SnS₂ nanosheets or nanoplates have exhibited high-mobility with large on-off ratios for field-effect transistors (FETs) [26], fast photo-response for photodetectors [15, 108] and large theoretical specific capacity for metal-ion batteries[12, 109, 110].

Therefore, it is essential to control the crystal phases of IVAMCs for further broadening their applications. Various methods such as mechanical exfoliation [26], vapor-transport

deposition (VTD) [100, 102, 111], and wet chemical synthesis [13, 112] have been employed for the preparation of monolayer or few-layer IVAMCs. In the following paragraphs, we will discuss the factors that control the crystal phase of the IVAMCs during or after growth, especially through the change of temperature [14, 113-115], using reducing agent [27] and e-beam irradiation[116].

3.1 Thermal effect

Temperature is always a deterministic factor affecting crystallization of materials. Taking SnS₂ as an example, previous reports suggested that low-temperature (e.g. < 600°C) synthesis is beneficial to the formation of the 2H-polytype, while intermediate temperatures favor the 18R phase and high temperatures above 800 °C lead to 4H-SnS₂. [99, 117] As for SnSe, which exhibits the low temperature orthorhombic phase and high temperature cubic phase[14, 118-120], Zhao et al. demonstrated the reversible phase transition between them by heating the sample from room temperature to ~800 K and then cooling it back to room temperature (Figure

9a-c).[14]

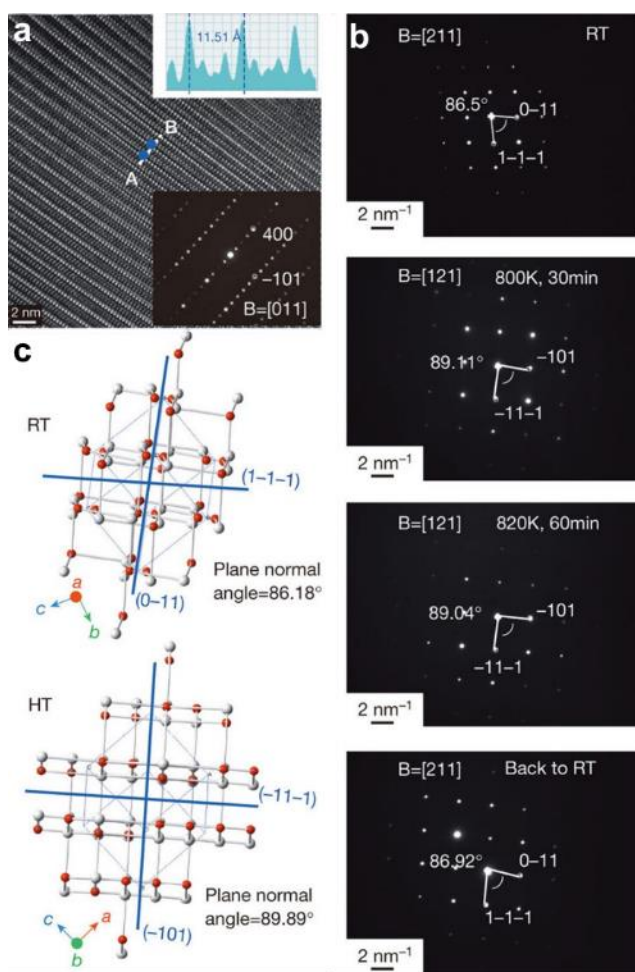


Figure 9 (a) Main panel, high-resolution transmission electron microscopy (HRTEM) image of single-crystal SnSe (scale bar, 2 nm). Bottom inset, corresponding diffraction pattern along the [011] zone axis; top inset, the line profile (distance is plotted in Å, y axis) along the dotted line AB in the main panel showing the d spacing of (100). (b) Simulated crystal structures of the

phase at room temperature (RT; Pnma) and at high temperature (HT; Cmcm), viewing along the [211] and [121] directions; planes (1-1-1), (-101) and (0-11) are marked by blue lines. (c) Diffraction patterns obtained at different temperatures. B, zone axis. There is a difference in measured angle between (1-1-1) and (0-11) of about 2.6° between room and elevated temperatures. Reproduced with permission from ref. [14]. Copyright 2014, Nature Publishing Group.

In addition, transition between MX and MX₂ can also be realized via temperature control. Fernandes et al. found that selenization of magnetron sputtered Sn at 300-470 °C favored the growth of hexagonal-phased SnSe₂, and at higher temperatures of ~530-570 °C, orthorhombic SnSe became the major product.[113] Similarly, Huang et al. reported the synthesis of diverse shaped and phased SnSe_x by controlling the substrate temperature in a CVD process.[114] As shown in Figure 10a-j, on the substrate near the high temperature zone, square-shaped orthorhombic SnSe nanosheets were obtained, and those on the substrate with lower temperatures, hexagonal, truncated triangular and triangular nanoplates in the hexagonal phase were synthesized. This phenomenon was attributed to the fact that, at higher temperatures, adsorbed Se atoms were likely desorbed more quickly into the carrier gas, which led to the formation of SnSe instead of SnSe₂.

Besides controlling the growth temperature, post-growth thermal annealing can cause phase transitions as well. For example, Zhou et al. heat-treated SnS₂ in Ar atmosphere and achieved SnS structures due to the depletion of S by partial sublimation and dissociation of SnS₂. [115] Importantly, by taking the advantage of the thermal induced phase transition, Tian et al. recently reported the creation of in-plane p-n heterostructures by selectively thermal conversion of SnSe₂ to SnSe in vacuum.[121] The junction between the hexagonal SnSe₂ and orthorhombic SnSe formed atomically sharp interface, as confirmed by scanning tunneling spectroscopy (STM) measurement. Notably, SnSe₂ was found to be heavily n-doped due to Se vacancies and interstitial Sn, whereas SnSe was p-doped due to Sn vacancies and interstitial Se.

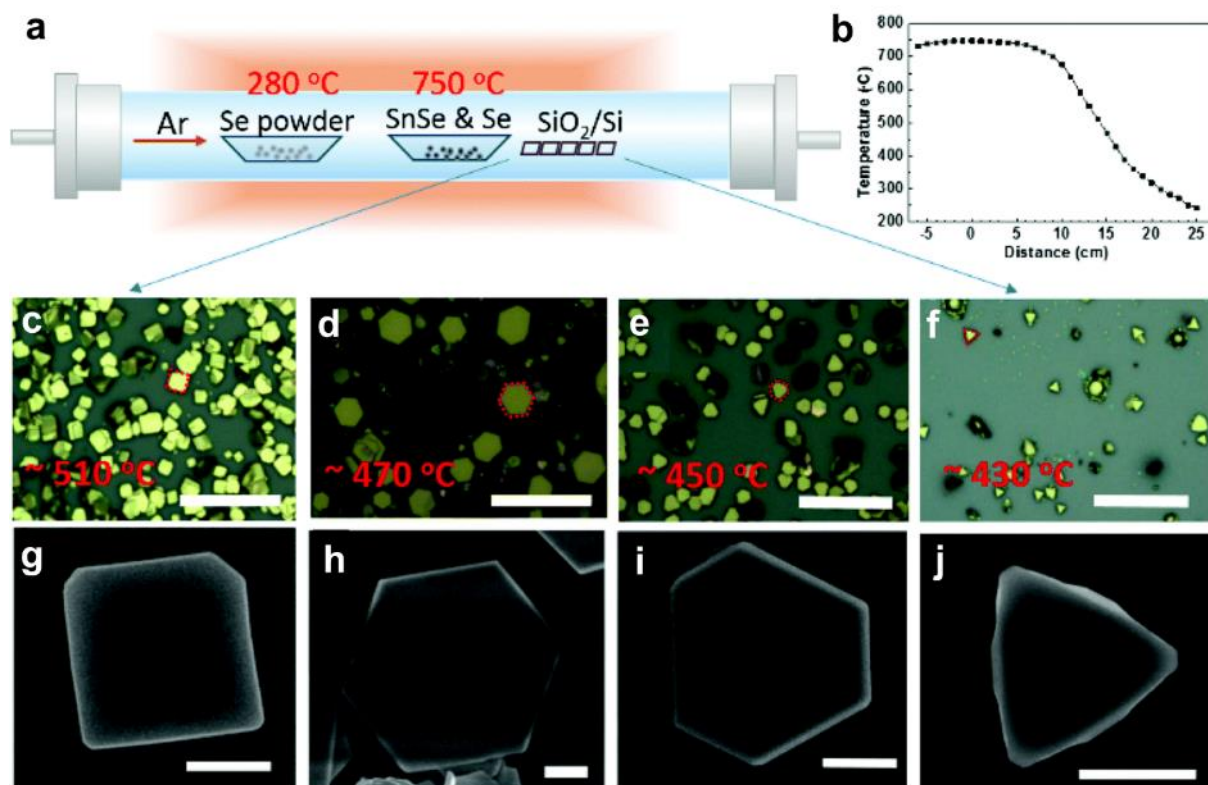


Figure 10 (a, b) The experimental setting and various nanosheets grown on SiO_2/Si substrates. (a) The schematic of the experimental setups. (b) The temperature gradient in the furnace. The middle of the second heating zone is defined as the origin. (c, d, e and f) The optical images of the as-grown nanosheets. Scale bar: 30 μm . (g, h, i and j) The corresponding SEM images of NSs. Scale bar: c, 0.5 μm ; e, g and i, 2 μm . Reproduced with permission from ref. [114]. Copyright 2015, The Royal Society of Chemistry.

3.2 Reducing environment

Given the fact that the oxidation state of Sn in SnS is +2, smaller than that in SnS_2 (+4), preferred growth of SnS may be achieved in a reducing environment. Recently, Ahn et al. reported the controllable CVD growth of hexagonal SnS_2 or orthorhombic SnS by altering the ratio of H_2/N_2 gas, which carried S vapor to react with SnO_2 on substrate (Figure 11a-f) [27]. It was found that rectangular SnS crystals were obtained when the H_2/N_2 ratio was larger than 0.4. Below that, the products became irregularly shaped. When no H_2 was introduced, hexagonal phased SnS_2 crystals in the triangular shape were obtained.

3.3 E-beam irradiation

It has been suggested that e-beam irradiation during transmission electron microscopy (TEM) analysis can cause a local temperature rise to ~ 500 °C. Recently, Sutter et al. reported electron-beam induced vacancy formation and transition of trigonal (1T) phased SnS_2 to orthorhombic SnS [116]. Few-layer SnS_2 was found to first transform to a Sn_2S_3 intermediate and then to SnS (Figure 12a-f). It is worth noting that the appearance of Sn_2S_3 intermediate caused rotational realignment of atoms and resulted in the tilted (21° off-axis) SnS. For ultrathin SnS_2 (< 3 layers), the Sn_2S_3 intermediate was not observed, leading to the formation of c-axis oriented SnS.

Similar to SnS_2 , SnSe_2 also underwent e-beam induced phase transition to SnSe, but without the formation of any Sn_2Se_3 intermediate. This observation was supported by phase diagrams previously created by Sharma et al. [122], which indicated that while Sn_2S_3 can exist under thermal equilibrium, Sn_2Se_3 can not.

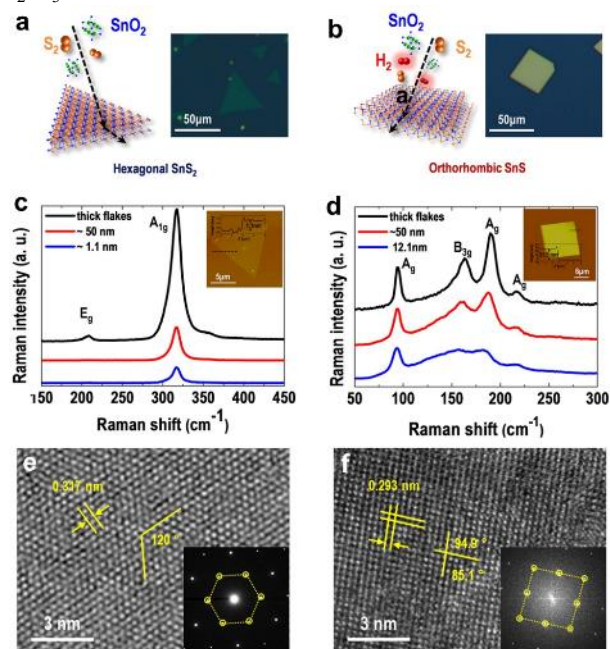


Figure 11 Growth schematics and representative optical microscope images of (a) hexagonal 2D SnS₂ in N₂ and (b) orthorhombic 2D SnS in N₂-H₂. Raman spectra of (c) SnS₂ 2D crystals and (d) SnS 2D crystals of various thickness. Insets: atomic force microscope images. HRTEM images of (e) a SnS₂ crystal and (f) a SnS crystal. The corresponding FFT-diffraction patterns of the insets clearly show the hexagonal and orthorhombic lattices. Reproduced with permission from ref. [27]. Copyright 2015, American Chemical Society.

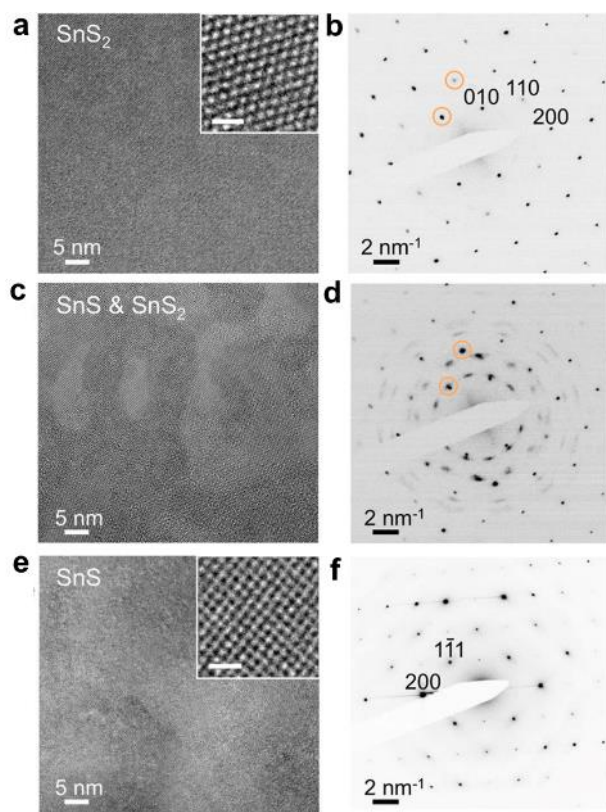


Figure 12 Evolution of few-layer SnS₂ under electron-beam irradiation. (a) HRTEM image of a thin area in a SnS₂ flake. (b) HRTEM image of the same flake after 200 keV electron-beam exposure at room temperature for 12 min. (c) TEM image of the flake after 200 keV electron-beam exposure at 300 °C for 36 min. (d) Electron diffraction pattern showing the SnS₂ crystal structure along [001] zone axis. (e) Diffraction pattern showing a superposition of the original SnS₂ reflections and additional reflections that can be indexed to the orthorhombic α -SnS crystal structure. (f) Diffraction pattern indexed to single crystalline orthorhombic α -SnS crystal structure along the [011] zone axis. Scale bars of panels a and c insets: 1 nm. Reproduced with permission from ref. [116]. Copyright 2016, American Chemical Society.

4 Noble metals

The progress made in graphene and 2D layered inorganic semiconductors has provoked research in other 2D systems. For example, noble metals in the 2D form have exhibited structural and chemical properties distinctive from their bulk counterparts, and found a wide range of applications such as energy conversion, surface enhanced Raman scattering, bio-sensing, photothermal therapy and catalysis.[17, 19, 20, 28, 29, 123-126]

The thermodynamically stable phases vary for different noble metals.[21] While Au, Ag, Pd, Pt, Rh and Ir normally

crystallize in the highly symmetric fcc structure, other metals, typically Ru and Os, prefer the hcp structure (Figure 13a). In addition to the commonly observed phases, i.e. fcc and hcp-2H, other phases including hcp-4H and face-centered tetragonal (fct) have also been identified in noble metals.[28, 29, 127] The fcc, 2H and 4H phases all belong to the close-packed systems, and only differ in the stacking sequence of the close-packed planes (Figure 13b).

As known, the functional properties of noble metal nanostructures can be tuned by their size [128], shape [129, 130], composition [131, 132] and crystal phase [127, 133, 134]. For instance, a thin film of 4H Ag showed over 100 times larger in-plane resistivity and much stronger visible-light absorption compared with that of the common fcc Ag films.[133] hcp Ru nanoparticles (NPs) are more active to catalyze CO oxidation than fcc Ru NPs with the similar size.[134] FePt NPs exhibited a property transition from superparamagnetic to strongly ferromagnetic when they underwent a transformation from fcc to an unusual fct structure.[127] Therefore, controlling the crystal structure of noble metals and understanding the mechanisms behind phase control are of paramount importance.

In the following context, we will discuss the effect of thickness,[28, 29, 135] surface ligands,[19, 29, 46, 136] metal coating [46, 137, 138] as well as pressure [39, 139] on the crystal phase of 2D noble metals.

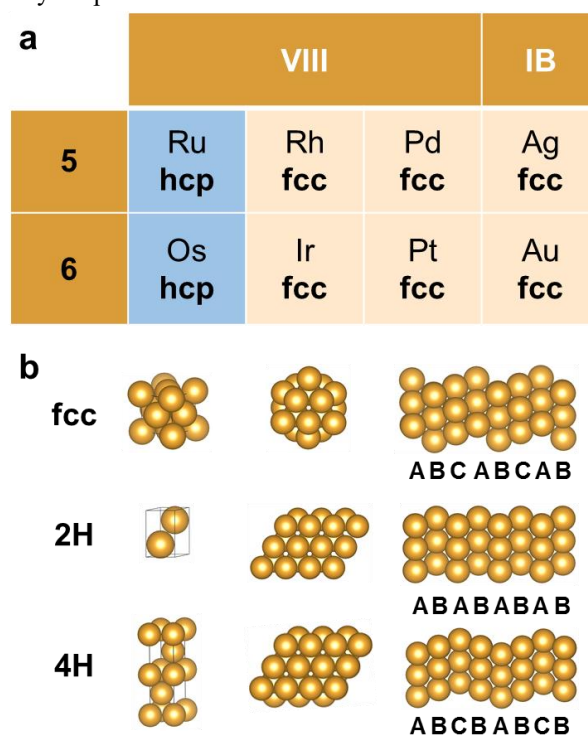


Figure 13 (a) Crystal phase periodic table for noble metals. (b) Structural models for fcc, 2H and 4H phases for noble metals. The left, middle and right columns show the unit cell 3-D view, close-packed plane top-view, and side-view showing the packing sequence of close-packed planes, respectively.

4.1 Size effect

Both theoretical and experimental investigations have showed that when one of the dimensions of a crystal is reduced to the nanoscale, its surface energy can dominate the total systemic energy and unusual crystals phases that are absent or metastable in the bulk form may be revealed.[128, 140, 141]

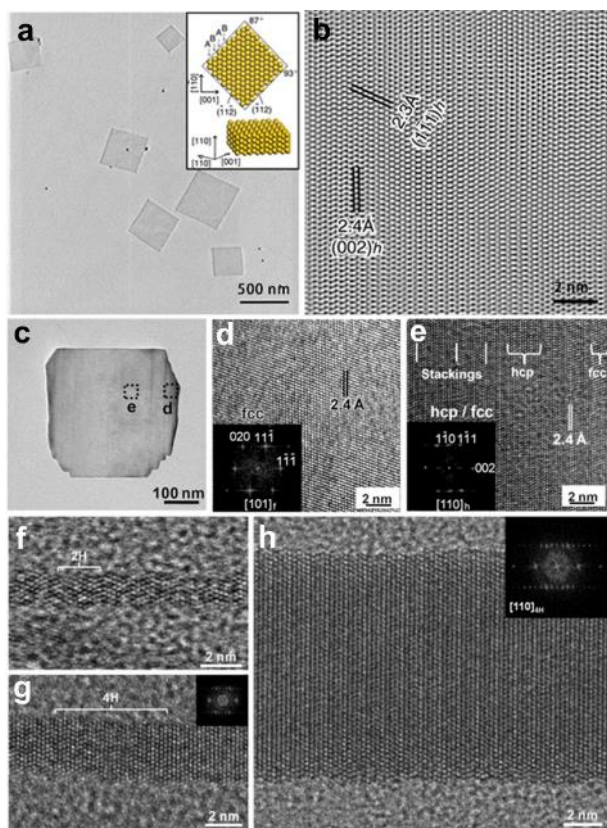


Figure 14 (a) TEM image of ~ 2.4 -nm thick AuSSs on a GO surface. (b) HRTEM image of a small region of a typical AuSS oriented normal to $[110]_h$. Reproduced with permission from ref. [28]. Copyright 2011, Nature Publishing Group. (c) TEM image of a typical AuSP synthesized on GO. (d, e) HRTEM images of the areas designated in (c). Insets in (d, e): Fast Fourier transform (FFT) generated selected area electron diffraction (SAED) patterns of the corresponding HRTEM images in (d, e). Reproduced with permission from ref. [135]. Copyright 2011, John Wiley & Sons, Inc. (f) 2H structure and stacking faults were observed at the reaction time of 4 h. (g) 4H structure appeared at the reaction time of 8 h. Inset: the corresponding FFT pattern of the marked 4H domain in g. (h) the 4H structure were obtained at the reaction time of 12 h. Inset: the corresponding FFT pattern of the HRTEM image shown in h. Reproduced with permission from ref. [29]. Copyright 2015, Nature Publishing Group.

This is elaborated in our previous reports on the synthesis of 2H phased ultrathin Au square sheets (AuSSs) and 4H phased Au nanoribbons (NRBs).[28, 29, 135] In the case of 2H AuSSs[28], they were synthesized from heating a mixture solution containing graphene oxide sheets, HAuCl_4 , oleylamine, hexane and ethanol at 55°C . The AuSSs exhibited an edge length of 200–500 nm and a thickness of only ~ 2.4 nm, corresponding to ~ 16 Au atomic layers (Figure 14a–b). Detailed TEM analyses proved that the AuSSs were pure hcp

structures. Importantly, by prolonging the growth time, when the thickness of an AuSS increased from ~ 2.4 to ~ 6 nm, fcc domains began to appear. Alternatively, the thickness of the hcp AuSSs could also be increased through a secondary growth of Au on them.[135] The obtained Au square-like plates demonstrated the alternating hcp/fcc structure in their center region with a thickness of ~ 5 nm and a pure fcc structure in their 7.3 nm-thick edge areas (Figure 14c–e), revealing a thickness-dependent structural property.

By introducing 1,2-dichloropropane to the growth solution containing HAuCl_4 , oleylamine and hexane, our group prepared ultrathin Au nanoribbons (NRBs) with an unprecedentedly observed 4H structure for Au.[46] The time-dependent characterization of intermediate products showed that ultrathin Au nanowires (Au NWs) with a diameter of 1.4–2.0 nm were formed first at the reaction time of 4 h, and showed short-range 2H structural domains along with many stacking faults (Figure 14f). As the reaction proceeded to 8 h, these Au NWs grew into ribbon-like nanostructures with a width of 2.8–5.8 nm (Figure 14g), and at this stage, hexagonal 4H domains already existed. The final Au NRBs with widths of 8.0–20.0 nm showed the 4H phase over their entire structures after 12 h of reaction (Figure 14h). The fact that the 2H structure gradually evolved to the 4H structure with increasing ribbon width suggests that the 4H Au is relatively more stable compared with the 2H Au. This agrees with previous theoretical calculations that 4H Au processes larger cohesive energy per atom than the 2H counterpart.[142]

Very recently, we also prepared ultrathin Ru nanoblades with an intergrown fcc/hcp structure by using Cu salt as a co-reduction and sacrificial reagent.[143] The Ru nanoblades with a thickness of ~ 2 nm showed basal planes normal to the close-packing $[111]_f$ or $[001]_h$ directions, suggesting a faulty stacking of the two phases. Control experiments further indicated that by annealing the ultrathin Ru nanoblades, they transformed into larger nanoparticles showing exclusively the thermodynamically stable hcp structure.

4.2 Ligand effect

Because the surface energy of an ultrathin nanostructure may dominate its total systemic energy, surface ligands are expected to exert crucial effects on its chemical and structural stability.[128, 144] In fact, the effect of size usually comes hand-in-hand with the effect of surface functionalization. Very recently, Li et al. solvothermally synthesized unusual hcp Rh nanosheets which were about 500–600 in edge length (Figure 15a–c).[19] Extended X-ray absorption fine structure (EXAFS) analysis of the nanosheets indicated that the Rh atoms possessed a small coordination number of ~ 6.4 , suggesting that they were single atomic layers. Theoretical calculations suggested that these single layer nanosheets were likely stabilized by the surface adsorbed polyvinylpyrrolidone (PVP) molecules which considerably decreased the surface energy of Rh from 0.126 to $0.071 \text{ eV } \text{\AA}^{-2}$. Evidently, without presence of PVP, Rh nanosheets were aggregated. In addition, CO molecules, which were produced via decomposition of formaldehyde in the growth solution at elevated temperatures,

were suggested to strongly interact and stabilize the Rh nanosheets. The use of CO as stabilizing agent has been demonstrated previously in the synthesis of ultrathin Pd nanosheets by Huang and coworkers.[17] In another report, by reducing $\text{Pt}(\text{acac})_2$ and $\text{Bi}(\text{NE})_3$ with oleylamine in the presence of NH_4Br , Hou et al. obtained colloidal of polycrystalline hcp BiPt nanoplates.[136] The BiPt nanoplates showed a lateral size of ~ 42 nm and a thickness of ~ 6 nm. Importantly, the Br ions were suggested to adsorb on the (101) planes of PtBi, preventing the nanostructures from growing along the [101] direction, and thus forming the anisotropic nanoplates. Besides, halide ions such as Cl^- or I^- except for F^- were found to exert the similar effect.

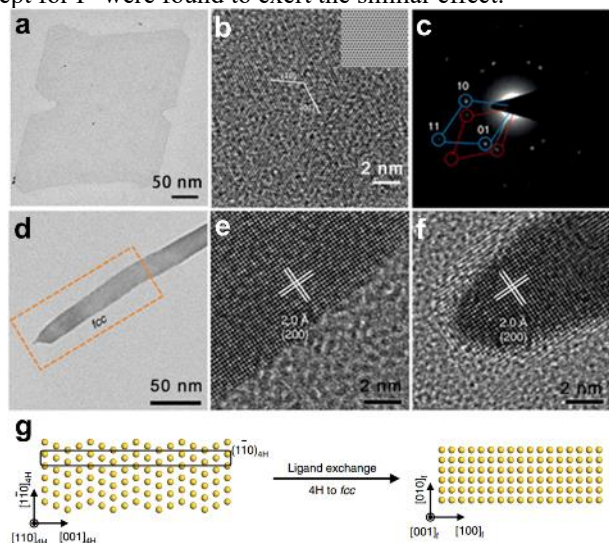


Figure 15 (a) High-magnification TEM images of hcp Rh nanosheets. (b) Aberration-corrected HRTEM image of hcp Rh nanosheets. Inset: the corresponding filtered HRTEM image using the crystallographic method. (c) A typical SAED pattern of hcp Rh nanosheets. Reproduced with permission from ref. [19]. Copyright 2014, Nature Publishing Group. (d) A typical TEM image of an Au NRB after the ligand exchange. (e-f) HRTEM images taken from the edge and end of the marked region in d, respectively (g) Schematic illustration of the ligand exchange induced phase transformation of 4H Au NRBs. Reproduced with permission from ref. [29]. Copyright 2015, Nature Publishing Group.

Because of the crucial effects of surface ligands, ligand exchange has been explored in order to control the crystal phase of ultrathin Au structures. For example, the aforementioned AuSSs were originally capped with oleylamine molecules from their synthetic solution. We found that if the oleylamine was replaced with thiols (e.g. octadecanethiol, ODT), which bond more strongly with Au surfaces by forming Au-S bonds, the hcp AuSSs were transformed to the pure fcc AuSSs with a [100] orientation showing the typical square lattice pattern.[46] Interestingly, this phase transition caused a thickness increase and lateral size reduction in AuSSs, due to the enlarged lattice spacing from the initial $d_{(110)_h} = 1.5$ Å to the final $d_{(200)_f} = 2.0$ Å if the number of atomic layers was kept consistent during the transition. It is worth noting that a sufficiently high concentration of ODT molecules in the solution is needed to ensure a rapid and complete exchange of oleylamine with ODT (≥ 20 mM), and thus

a uniform phase transformation over the entire structure of the hcp AuSS. Otherwise, poorly crystallized Au nanostructures with irregular shapes were obtained, probably due to non-uniform ligand exchange induced in-plane strain. The thiols that can induce phase transformation of AuSSs are not limited to ODTs, but other thiols regardless of the lengths of n-alkane chains ($3 < n < 18$), the functional groups (carboxylic acid, hydroxide or benzene), and the number of thiol groups (monothiol or dithiol), can also be used.

Similarly, by applying ligand exchange, transformation of the 4H Au NRBs to the fcc NRBs was also realized.[46] The TEM images of the resulting fcc NRBs and the transformation schemes are shown in Figure 15d-g. From the scheme we can see that, the transition of 4H-to-fcc transition can be described as the flattening of the $(1-10)_{4H}$ planes. This observation agrees with previous findings that thiols (or sulfur-containing molecules) can bond with surface Au atoms and induce their reconstruction to generate a metal layer with higher coordination number.[145, 146]

4.3 Metal coating

The surface properties of metal structures could be significantly altered by epitaxially depositing a different metal.[147-149] Note that this strategy has recently been applied to realize various bimetallic nanomaterials with controllable crystal phases, e.g. hcp/fcc or fcc Au@Ag square sheets,[46] fcc Au@M (M = Pt, Pd) rhombic nanoplates,[137] 4H/fcc Au@M NRBs (M = Ag, Pd, Pt),[46] as well as 4H/fcc Au@M (M = Ir, Rh, Os, Ru and Cu).[138]

Taking hcp AuSSs as an example, depositing Ag on its surface can result in two different types of phase transformation depending on the kind of reducing agent used for Ag reduction.[46] In the case of using reducing agents such as L-ascorbic acid or NaBH_4 , the pure hcp AuSSs were transformed to the pure $(100)_f$ -oriented fcc Au@Ag core-shell square sheets based on TEM, HRTEM, SAED and energy dispersive X-ray spectrometry (EDS) analyses (Figure 16a-d). This kind of transition proceeds via the flattening of the $(1\bar{1}0)_{2H}$ planes, which assembles that of ligand exchange induced phase transition mentioned above. In contrast, when oleylamine was used to reduce Ag, hcp AuSSs were grown into the $(110)_h/(101)_f$ -oriented hcp/fcc mixed Au@Ag nanosheets (Figure 16f-i). This type of phase transformation proceeds via the change of packing sequence of closed-packed planes, similar to the martensitic transition, leading to an intergrowth of hcp and fcc domains.[28, 135] Importantly, it was also found that the mixed hcp/fcc Au@Ag square sheets could be obtained by using octylamine (a primary amine), whereas the reduction with dioctylamine (a secondary amine) led to the formation of pure fcc $(100)_f$ -oriented Au@Ag nanosheets. These experimental results suggested that primary amines may favor the formation of hcp-containing structures.[150, 151]

Interestingly, unlike coating hcp AuSSs with Ag, which resulted in either the $(100)_f$ -oriented or $(110)_h/(101)_f$ -oriented hcp/fcc mixed Au@Ag nanosheets, coating AuSSs with Pt and Pd led to the production of fcc Au@Pt and Au@Pd core-

shell rhombic nanoplates with high density of twins and stacking faults (Figure 16j-n).[137] This difference might be due to the larger lattice mismatch between Pt or Pd and Au (~5.8%), compared to that between Ag and Au (~0.2%). Note that a small amount of fcc (100)_f-oriented Au@Pt or Au@Pd square nanoplates (< 10% yield) was also obtained in the final products.

In addition to hcp AuSSs, 4H Au NRBs have also been used to prepare bimetallic structures, namely 4H/fcc Au@M

(M=Ag, Pt, Pd as well as Ir, Rh, Os, Ru and Cu) structures.[29, 138] However, a complete phase transition from 4H to fcc structures was not observed in these attempts, and mixed 4H/fcc Au@M NRBs were mostly obtained, indicating that 4H Au nanostructures are relatively more stable than that of hcp (2H) phase. This was also reflected from our previous findings that 2H Au nanosheets or nanowires were more easily destroyed under e-beam irradiation compared to 4H nanoribbons.[28, 152]

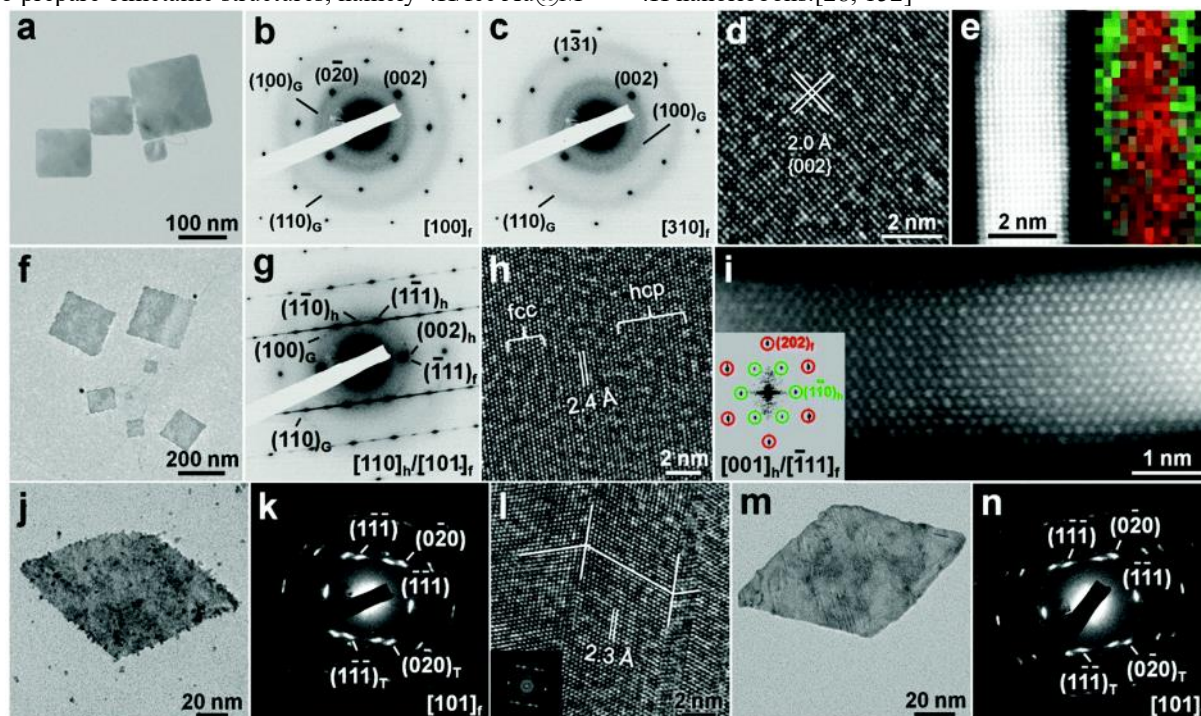


Figure 16 (a) Bright-field TEM image of typical fcc Au@Ag square sheets on GO sheets. (b and c) SAED patterns taken along the $[100]_f$ (b) and $[310]_f$ (c) zone axes of an fcc Au@Ag square sheet. (d) A typical HRTEM image of fcc Au@Ag square sheet. (e) Aberration-corrected high-angle annular dark-field scanning transmission electron microscopy (HAADF-STEM) image and the corresponding overlapped STEM-EDS elemental mapping (Au: red color; Ag: green color) showing the cross-section of a typical fcc Au@Ag square sheet. (f) Bright-field TEM image of typical hcp/fcc Au@Ag square sheets on GO sheets. (g) SAED pattern and (h) HRTEM image of a representative hcp/fcc Au@Ag square sheet. (i) Aberration-corrected HAADF-STEM image of the cross-section of an hcp/fcc Au@Ag square sheet collected along the $[001]_h/[111]_f$ zone axes. Inset: the corresponding FFT pattern of the HAADF-STEM image shown in (i). Reproduced with permission from ref. [46]. Copyright 2015, Nature Publishing Group. (j) TEM image, (k) SAED pattern and (l) HRTEM image of a typical fcc Au@Pt rhombic nanoplate. Inset in (l): the corresponding FFT pattern of the HRTEM image shown in (l). (m) TEM image and (n) the corresponding SAED pattern of a typical fcc Au@Pd rhombic nanoplate. Reproduced with permission from ref. [137]. Copyright 2015, John Wiley & Sons, Inc.

4.4 High pressure

High pressure has enabled phase transition in many materials such as TMDs [40, 153], GaAs [154] and BiTeI [155, 156]. Normally, bulk crystals of noble metals show good tolerance towards moderate pressures, largely due to their highly symmetric and close-packed crystalline structures. For instance, submillimeter fcc crystals of Ag, Au, Pt, Pd, and Cu are stable when subjected to pressure up to 91.8, 182, 304, 77.4, and 188 GPa, respectively, at room temperature.[157, 158] However, nanostructured noble metals are more prone to pressure induced structural change.[39, 139, 159] For example, Sun et al. reported the preparation of Ag nanoplates based on a galvanic reaction between a heavily doped n-type GaAs wafer and AgNO₃ aqueous solution. The nanoplates exhibited multiple hcp twin planes in the dominating fcc structure [39]. Un-

der increasing pressure up to 1.03 GPa, the hcp domains associated with the twin planes disappeared to give a pure fcc structure as evidenced in the XRD pattern (Figure 17a). During this process, the Ag nanoplates were broken into smaller domains (typically < 50 nm), resulting in the loss of the multiple twin planes (Figure 17b). The fractured Ag nanocrystals further transformed to fct structures as the pressure was further increased up to 12 GPa.

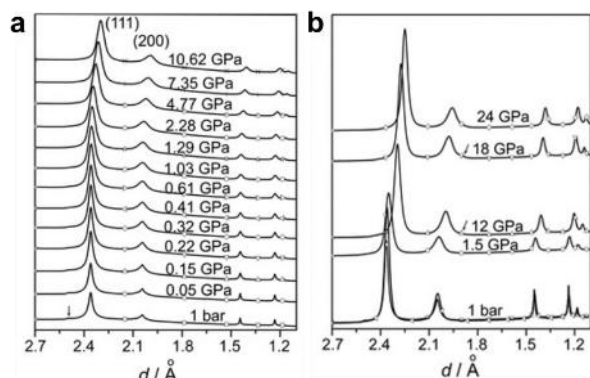


Figure 17 (a) XRD patterns of the as-grown Ag nanoplates on the wafer obtained during compression with small steps. (b) XRD patterns obtained with large steps. Reproduced with permission from ref. [39]. Copyright 2011, John Wiley & Sons, Inc.

5 Conclusions

In summary, we have discussed the recent development of strategies used for the crystal-phase controlled growth or post-growth treatment of 2D TMDs, VIAMDS and noble metals. For TMDs, their phase transition can be realized via ion intercalation, alloying/doping, electron injection, electrostatic gating, defect engineering, strain engineering and so on. In contrast, the crystal-phase control of IVAMCs has been mostly relying on thermal methods. Although solid-state phase diagrams can guide the variation of temperature, other factors such as growth substrate, use of reducing agent, amount of and ratio between reactants could also affect the final products. Defects such as chalcogen vacancies could be created via thermal treatment as well as e-beam irradiation, leading to the stoichiometric transition from MX_2 to MX . As for 2D noble metals, in addition to conventional strategies involving high energies, such as high pressure and high temperature treatment, exchange of surface ligands and secondary growth of similar metals can be easily implemented to induce phase transitions at milder conditions.

In spite of the progress made in this research direction, challenges remain to be resolved. Stability is one of the most important issues, as the metastable crystal structures might revert back to the thermodynamically stable ones under the influence of high temperature or other external perturbations. Although surface functionalization can modify their surface energy and improve stability, it severely sacrifices their functional performances, especially in applications that require surface activity. As another issue, currently, the phase control in most TMDs relies on post-growth strategies. Although the scalable and controlled synthesis of 1T'- $\text{MoS}(\text{Se})_2$ has been reported recently [72], the development of direct phase-controlled synthesis methods for other materials needs continuous efforts. Very differently, for 2D noble metals, their uncommon phases have only been realized via direct growth under specific synthesis conditions. In other words, transfor-

mation from their thermodynamic stable structures to metastable ones has not been achieved via post-growth methods. Nevertheless, reversible transition of spherical Pd nanoparticles from crystalline to amorphous state has been observed previously via ligand exchange between trioctylphosphine and oleylamine.[151] This suggests the possibility of achieving the reversible phase transition in 2D noble metals, which requires further investigations.

Furthermore, although polymorphism has been observed in other nanostructures such as semiconducting III-V compounds (e.g. InAs, GaAs) and II-VI compounds (e.g. ZnS, CdSe),[160, 161] few reports have been on the 2D form of these materials as well as their phase controlled syntheses, which are interesting to be explored in future.

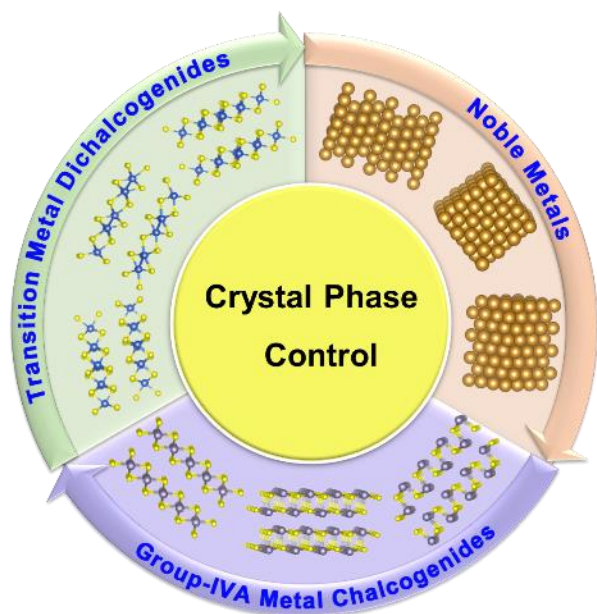
Lastly, it is interesting that unusual phased noble metals can be used as substrates to guide the epitaxial growth of other metals to achieve unusual crystal structures that cannot be achieved by other means.[162-165] Such strategy may be extended to TMDs and other layered materials. More importantly, epitaxial growth between different low-dimensional material systems may provide opportunities to further expand the map of crystal phases.

Acknowledgments

This research was supported by the Joint Research Fund for Overseas Chinese, Hong Kong and Macao Scholars (Grant No. 51528201). H.Z. thanks the support from MOE under AcRF Tier 2 (ARC 19/15, No. MOE2014-T2-2-093; MOE2015-T2-2-057; MOE2016-T2-2-103; MOE2017-T2-1-162) and AcRF Tier 1 (2016-T1-001-147; 2016-T1-002-051; 2017-T1-001-150; 2017-T1-002-119), and NTU under Start-Up Grant (M4081296.070.500000) in Singapore.

Conflict of interest The authors declare that they have no conflict of interest.

Table of Contents graphic



- Novoselov KS, Fal' Ko VI, Colombo L, Gellert PR, Schwab MG, Kim K. A roadmap for graphene. *Nature*, 2012, 490: 192-200
- Novoselov KS, Geim AK, Morozov SV, Jiang D, Zhang Y, Dubonos SV, Grigorieva IV, Firsov AA. Electric Field Effect in Atomically Thin Carbon Films. *Science*, 2004, 306: 666-669
- Schwierz F. Graphene transistors. *Nat Nanotechnol*, 2010, 5: 487-496
- Chhowalla M, Shin HS, Eda G, Li L-J, Loh KP, Zhang H. The chemistry of two-dimensional layered transition metal dichalcogenide nanosheets. *Nat Chem*, 2013, 5: 263-275
- Manzeli S, Ovchinnikov D, Pasquier D, Yazyev OV, Kis A. 2D transition metal dichalcogenides. *Nat Rev Mater*, 2017, 2: 17033-17047
- Tan C, Zhang H. Two-dimensional transition metal dichalcogenide nanosheet-based composites. *Chem Soc Rev*, 2015, 44: 2713-2731
- Wang QH, Kalantar-Zadeh K, Kis A, Coleman JN, Strano MS. Electronics and optoelectronics of two-dimensional transition metal dichalcogenides. *Nat Nanotechnol*, 2012, 7: 699-712
- Zhang X, Lai Z, Ma Q, Zhang H. Novel structured transition metal dichalcogenide nanosheets. *Chem Soc Rev*, 2018, 47: 3301-3338
- Fiori G, Bonaccorso F, Iannaccone G, Palacios T, Neumaier D, Seabaugh A, Banerjee SK, Colombo L. Electronics based on two-dimensional materials. *Nat Nanotechnol*, 2014, 9: 768-779
- Tan CL, Cao XH, Wu XJ, He QY, Yang J, Zhang X, Chen JZ, Zhao W, Han SK, Nam GH, Sindoro M, Zhang H. Recent Advances in Ultrathin Two-Dimensional Nanomaterials. *Chem Rev*, 2017, 117: 6225-6331
- Xu M, Liang T, Shi M, Chen H. Graphene-Like Two-Dimensional Materials. *Chem Rev*, 2013, 113: 3766-3798
- Seo Jw, Jang Jt, Park Sw, Kim C, Park B, Cheon J. Two-Dimensional SnS₂ Nanoplates with Extraordinary High Discharge Capacity for Lithium Ion Batteries. *Adv Mater*, 2008, 20: 4269-4273
- Li L, Chen Z, Hu Y, Wang X, Zhang T, Chen W, Wang Q. Single-Layer Single-Crystalline SnSe Nanosheets. *J Am Chem Soc*, 2013, 135: 1213-1216
- Zhao L-D, Lo S-H, Zhang Y, Sun H, Tan G, Uher C, Wolverton C, Dravid VP, Kanatzidis MG. Ultralow thermal conductivity and high thermoelectric figure of merit in SnSe crystals. *Nature*, 2014, 508: 373-377
- Xia J, Zhu D, Wang L, Huang B, Huang X, Meng XM. Large-Scale Growth of Two-Dimensional SnS₂ Crystals Driven by Screw Dislocations and Application to Photodetectors. *Adv Funct Mater*, 2015, 25: 4255-4261
- Wang XT, Li YY, Huang L, Jiang XW, Jiang L, Dong HL, Wei ZM, Li JB, Hu WP. Short-Wave Near-Infrared Linear Dichroism of Two-Dimensional Germanium Selenide. *J Am Chem Soc*, 2017, 139: 14976-14982
- Huang X, Tang S, Mu X, Dai Y, Chen G, Zhou Z, Ruan F, Yang Z, Zheng N. Freestanding palladium nanosheets with plasmonic and catalytic properties. *Nat Nanotechnol*, 2010, 6: 28-32
- Cheng L, Wang C, Feng LZ, Yang K, Liu Z. Functional Nanomaterials for Phototherapies of Cancer. *Chem Rev*, 2014, 114: 10869-10939
- Duan H, Yan N, Yu R, Chang C-R, Zhou G, Hu H-S, Rong H, Niu Z, Mao J, Asakura H, Tanaka T, Dyson PJ, Li J, Li Y. Ultrathin rhodium nanosheets. *Nat Commun*, 2014, 5: 3093-3100
- Chen AC, Ostrom C. Palladium-Based Nanomaterials: Synthesis and Electrochemical Applications. *Chem Rev*, 2015, 115: 11999-12044
- Fan Z, Zhang H. Crystal phase-controlled synthesis, properties and applications of noble metal nanomaterials. *Chem Soc Rev*, 2016, 45: 63-82
- Zhou X, Zhang Q, Gan L, Li HQ, Xiong J, Zhai TY. Booming Development of Group IV-VI Semiconductors: Fresh Blood of 2D Family. *Adv Sci*, 2016, 3: 1600177-1600196
- Trigunayat GC. A survey of the phenomenon of polytypism in crystals. *Solid State Ionics*, 1991, 48: 3-70
- Wilson JA, Di Salvo FJ, Mahajan S. Charge-Density Waves in Metallic, Layered, Transition-Metal Dichalcogenides. *Phys Rev Lett*, 1974, 32: 882-885
- Wilson JA, Salvo FJD, Mahajan S. Charge-density waves and superlattices in the metallic layered transition metal dichalcogenides. *Adv Phys*, 1975, 24: 1171-1248
- Huang Y, Sutter E, Sadowski JT, Cotlet M, Monti OLA, Racke DA, Neupane MR, Wickramaratne D, Lake RK, Parkinson BA, Sutter P. Tin Disulfide—An Emerging Layered Metal Dichalcogenide Semiconductor: Materials Properties and Device Characteristics. *ACS Nano*, 2014, 8: 10743-10755
- Ahn J-H, Lee M-J, Heo H, Sung JH, Kim K, Hwang H, Jo M-H. Deterministic Two-Dimensional Polymorphism Growth of Hexagonal n-Type SnS₂ and Orthorhombic p-Type SnS Crystals. *Nano Lett*, 2015, 15: 3703-3708
- Huang X, Li SZ, Huang YZ, Wu SX, Zhou XZ, Li SZ, Gan CL, Boey F, Mirkin CA, Zhang H. Synthesis of hexagonal close-packed gold nanostructures. *Nat Commun*, 2011, 2: 292-297
- Fan Z, Bosman M, Huang X, Huang D, Yu Y, Ong KP, Akimov YA, Wu L, Li B, Wu J, Huang Y, Liu Q, Eng Png C, Lip Gan C, Yang P, Zhang H. Stabilization of 4H hexagonal phase in gold nanoribbons. *Nat Commun*, 2015, 6: 7684-7691
- Cao Y, Fatemi V, Fang S, Watanabe K, Taniguchi T, Kaxiras E, Jarillo-Herrero P. Unconventional superconductivity in magic-angle graphene superlattices. *Nature*, 2018, 556: 43
- Mcdonnell S, Addou R, Buie C, Wallace RM, Hinkle CL. Defect-Dominated Doping and Contact Resistance in MoS₂. *ACS Nano*, 2014, 8: 2880-2888
- Zhu J, Wang Z, Yu H, Li N, Zhang J, Meng J, Liao M, Zhao J, Lu X, Du L, Yang R, Shi D, Jiang Y, Zhang G. Argon Plasma Induced Phase Transition in Monolayer MoS₂. *J Am Chem Soc*, 2017, 139: 10216-10219
- Voiry D, Goswami A, Kappera R, Silva CdCCe, Kaplan D, Fujita T, Chen M, Asefa T, Chhowalla M. Covalent functionalization of monolayered transition metal dichalcogenides by phase engineering. *Nat Chem*, 2014, 7: 45-49
- Benson EE, Zhang H, Schuman SA, Nanayakkara SU, Bronstein ND, Ferrere S, Blackburn JL, Miller EM. Balancing the Hydrogen Evolution Reaction, Surface Energetics, and Stability of Metallic MoS₂ Nanosheets via Covalent Functionalization. *J Am Chem Soc*, 2018, 140: 441-450
- Li Y, Duerloo KAN, Wauson K, Reed EJ. Structural semiconductor-to-semimetal phase transition in two-dimensional materials induced by electrostatic gating. *Nat Commun*, 2016, 7: 8-15
- Wang Y, Xiao J, Zhu HY, Li Y, Alsaied Y, Fong KY, Zhou Y, Wang SQ, Shi W, Wang Y, Zettl A, Reed EJ, Zhang X. Structural phase transition in monolayer MoTe₂ driven by electrostatic doping. *Nature*, 2017, 550: 487-491
- Eda G, Yamaguchi H, Voiry D, Fujita T, Chen M, Chhowalla M. Photoluminescence from Chemically Exfoliated MoS₂. *Nano Lett*, 2011, 11: 5111-5116
- Fan X, Xu P, Zhou D, Sun Y, Li YC, Nguyen MAT, Terrones M, Mallouk TE. Fast and Efficient Preparation of Exfoliated 2H MoS₂ Nanosheets by Sonication-Assisted Lithium Intercalation and Infrared Laser-Induced 1T to 2H Phase Reversion. *Nano Lett*, 2015, 15: 5956-5960
- Sun Y, Yang W, Ren Y, Wang L, Lei C. Multiple-Step Phase Transformation in Silver Nanoplates Under High Pressure. *Small*, 2011, 7: 606-611

- 40 Nayak AP, Bhattacharyya S, Zhu J, Liu J, Wu X, Pandey T, Jin C, Singh AK, Akinwande D, Lin J-F. Pressure-induced semiconducting to metallic transition in multilayered molybdenum disulphide. *Nat Commun*, 2014, 5: 3731-3739
- 41 Zeng Z, Sun T, Zhu J, Huang X, Yin Z, Lu G, Fan Z, Yan Q, Hng HH, Zhang H. An Effective Method for the Fabrication of Few-Layer-Thick Inorganic Nanosheets. *Angew Chem Int Ed*, 2012, 51: 9052-9056
- 42 Liu Q, Li X, Xiao Z, Zhou Y, Chen H, Khalil A, Xiang T, Xu J, Chu W, Wu X, Yang J, Wang C, Xiong Y, Jin C, Ajayan PM, Song L. Stable Metallic 1T-WS₂ Nanoribbons Intercalated with Ammonia Ions: The Correlation between Structure and Electrical/Optical Properties. *Adv Mater*, 2015, 27: 4837-4844
- 43 Kochat V, Apte A, Hachtel JA, Kumazoe H, Krishnamoorthy A, Susarla S, Idrobo JC, Shimojo F, Vashishta P, Kalia R, Nakano A, Tiwary CS, Ajayan PM. Re Doping in 2D Transition Metal Dichalcogenides as a New Route to Tailor Structural Phases and Induced Magnetism. *Adv Mater*, 2017, 29: 1703754-1703761
- 44 Rhodes D, Chenet DA, Janicek BE, Nyby C, Lin Y, Jin W, Edelberg D, Mannebach E, Finney N, Antony A, Schiros T, Klarr T, Mazzoni A, Chin M, Chiu YC, Zheng W, Zhang QR, Ernst F, Dadayp JI, Tong X, Ma J, Lou R, Wan S, Qian T, Ding H, Osgood RM, Paley DW, Lindenberg AM, Huang PY, Pasupathy AN, Dubey M, Hone J, Balicas L. Engineering the Structural and Electronic Phases of MoTe₂ through W Substitution. *Nano Lett*, 2017, 17: 1616-1622
- 45 Kang Y, Najmaei S, Liu Z, Bao Y, Wang Y, Zhu X, Halas NJ, Nordlander P, Ajayan PM, Lou J, Fang Z. Plasmonic Hot Electron Induced Structural Phase Transition in a MoS₂ Monolayer. *Adv Mater*, 2014, 26: 6467-6471
- 46 Fan Z, Huang X, Han Y, Bosman M, Wang Q, Zhu Y, Liu Q, Li B, Zeng Z, Wu J, Shi W, Li S, Gan CL, Zhang H. Surface modification-induced phase transformation of hexagonal close-packed gold square sheets. *Nat Commun*, 2015, 6: 6571-6579
- 47 Splendiani A, Sun L, Zhang Y, Li T, Kim J, Chim C-Y, Galli G, Wang F. Emerging Photoluminescence in Monolayer MoS₂. *Nano Lett*, 2010, 10: 1271-1275
- 48 Cao T, Wang G, Han W, Ye H, Zhu C, Shi J, Niu Q, Tan P, Wang E, Liu B. Valley-selective circular dichroism of monolayer molybdenum disulphide. *Nat Commun*, 2012, 3: 887-891
- 49 Mak KF, He K, Shan J, Heinz TF. Control of valley polarization in monolayer MoS₂ by optical helicity. *Nat Nanotechnol*, 2012, 7: 494-498
- 50 Zeng H, Dai J, Yao W, Xiao D, Cui X. Valley polarization in MoS₂ monolayers by optical pumping. *Nat nanotechnol*, 2012, 7: 490-493
- 51 Lukowski MA, Daniel AS, Meng F, Forticaux A, Li L, Jin S. Enhanced Hydrogen Evolution Catalysis from Chemically Exfoliated Metallic MoS₂ Nanosheets. *J Am Chem Soc*, 2013, 135: 10274-10277
- 52 Voiry D, Yamaguchi H, Li J, Silva R, Alves DCB, Fujita T, Chen M, Asefa T, Shenoy VB, Eda G, Chhowalla M. Enhanced catalytic activity in strained chemically exfoliated WS₂ nanosheets for hydrogen evolution. *Nat Mater*, 2013, 12: 850-855
- 53 Wang H, Lu Z, Xu S, Kong D, Cha JJ, Zheng G, Hsu P-C, Yan K, Bradshaw D, Prinz FB, Cui Y. Electrochemical tuning of vertically aligned MoS₂ nanofilms and its application in improving hydrogen evolution reaction. *Proc Natl Acad Sci*, 2013, 110: 19701-19706
- 54 Bertolazzi S, Brivio J, Kis A. Stretching and Breaking of Ultrathin MoS₂. *ACS Nano*, 2011, 5: 9703-9709
- 55 Castellanos-Gomez A, Poot M, Steele Gary A, Van Der Zant Herre SJ, Agrañt N, Rubio - Bollinger G. Elastic Properties of Freely Suspended MoS₂ Nanosheets. *Adv Mater*, 2012, 24: 772-775
- 56 Velusamy DB, Kim RH, Cha S, Huh J, Khazaeinezhad R, Kassani SH, Song G, Cho SM, Cho SH, Hwang I, Lee J, Oh K, Choi H, Park C. Flexible transition metal dichalcogenide nanosheets for band-selective photodetection. *Nat Commun*, 2015, 6: 8063-8073
- 57 Huang X, Zeng Z, Zhang H. Metal dichalcogenide nanosheets: preparation, properties and applications. *Chem Soc Rev*, 2013, 42: 1934-1946
- 58 Wilson JA, Yoffe AD. The transition metal dichalcogenides discussion and interpretation of the observed optical, electrical and structural properties. *Adv Phys*, 1969, 18: 193-335
- 59 Fei Z, Palomaki T, Wu S, Zhao W, Cai X, Sun B, Nguyen P, Finney J, Xu X, Cobden DH. Edge conduction in monolayer WTe₂. *Nat Phys*, 2017, 13: 677-682
- 60 Ma X, Guo P, Yi C, Yu Q, Zhang A, Ji J, Tian Y, Jin F, Wang Y, Liu K, Xia T, Shi Y, Zhang Q. Raman scattering in the transition-metal dichalcogenides of 1T'-MoTe₂, T₁-MoTe₂, and T₂-WTe₂. *Phys Rev B*, 2016, 94: 214105-214112
- 61 Duerloo K-AN, Li Y, Reed EJ. Structural phase transitions in two-dimensional Mo- and W-dichalcogenide monolayers. *Nat Commun*, 2014, 5: 4214-4222
- 62 Keum DH, Cho S, Kim JH, Choe D-H, Sung H-J, Kan M, Kang H, Hwang J-Y, Kim SW, Yang H, Chang KJ, Lee YH. Bandgap opening in few-layered monoclinic MoTe₂. *Nat Phys*, 2015, 11: 482-486
- 63 Radisavljevic B, Radenovic A, Brivio J, Giacometti V, Kis A. Single-layer MoS₂ transistors. *Nat Nanotechnol*, 2011, 6: 147-151
- 64 Baugher BWH, Churchill HOH, Yang Y, Jarillo-Herrero P. Intrinsic Electronic Transport Properties of High-Quality Monolayer and Bilayer MoS₂. *Nano Lett*, 2013, 13: 4212-4216
- 65 Kibsgaard J, Chen Z, Reinecke BN, Jaramillo TF. Engineering the surface structure of MoS₂ to preferentially expose active edge sites for electrocatalysis. *Nat Mater*, 2012, 11: 963-969
- 66 Cho S, Kim S, Kim JH, Zhao J, Seok J, Keum DH, Baik J, Choe D-H, Chang KJ, Suenaga K, Kim SW, Lee YH, Yang H. Phase patterning for ohmic homojunction contact in MoTe₂. *Science*, 2015, 349: 625-628
- 67 Kappera R, Voiry D, Yalcin SE, Branch B, Gupta G, Mohite AD, Chhowalla M. Phase-engineered low-resistance contacts for ultrathin MoS₂ transistors. *Nat Mater*, 2014, 13: 1128-1134
- 68 Yoshida M, Ye J, Zhang Y, Imai Y, Kimura S, Fujiwara A, Nishizaki T, Kobayashi N, Nakano M, Iwasa Y. Extended Polymorphism of Two-Dimensional Material. *Nano Lett*, 2017, 17: 5567-5571
- 69 Zeng Z, Yin Z, Huang X, Li H, He Q, Lu G, Boey F, Zhang H. Single-Layer Semiconducting Nanosheets: High-Yield Preparation and Device Fabrication. *Angew Chem Int Ed*, 2011, 50: 11093-11097
- 70 Yang K, Wang XS, Li H, Chen B, Zhang X, Li SZ, Wang N, Zhang H, Huang X, Huang W. Composition- and phase-controlled synthesis and applications of alloyed phase heterostructures of transition metal disulphides. *Nanoscale*, 2017, 9: 5102-5109
- 71 Li H, Chen S, Jia X, Xu B, Lin H, Yang H, Song L, Wang X. Amorphous nickel-cobalt complexes hybridized with 1T-phase molybdenum disulfide via hydrazine-induced phase transformation for water splitting. *Nat Commun*, 2017, 8: 15377-15387
- 72 Yu Y, Nam G-H, He Q, Wu X-J, Zhang K, Yang Z, Chen J, Ma Q, Zhao M, Liu Z, Ran F-R, Wang X, Li H, Huang X, Li B, Xiong Q, Zhang Q, Liu Z, Gu L, Du Y, Huang W, Zhang H. High phase-purity 1T'-MoS₂ and 1T'-MoSe₂-layered crystals. *Nat Chem*, 2018, 10: 638-643
- 73 Yu P, Lin JH, Sun LF, Le QL, Yu XC, Gao GH, Hsu CH, Wu D, Chang TR, Zeng QS, Liu FC, Wang QJ, Jeng HT, Lin H, Trampert A, Shen ZX, Suenaga K, Liu Z. Metal-Semiconductor Phase-Transition in WSe_{2(1-x)Te_{2x}} Monolayer. *Adv Mater*, 2017, 29: 1603991-1603998
- 74 Lin Y-C, Dumcenco DO, Huang Y-S, Suenaga K. Atomic mechanism of the semiconducting-to-metallic phase transition in single-layered MoS₂. *Nat Nanotechnol*, 2014, 9: 391-396
- 75 Zhou L, Zubair A, Wang ZQ, Zhang X, Ouyang FP, Xu K, Fang WJ, Ueno K, Li J, Palacios T, Kong J, Dresselhaus MS. Synthesis of High-Quality Large-Area Homogenous 1T' MoTe₂ from Chemical Vapor Deposition. *Adv Mater*, 2016, 28: 9526-9531
- 76 Song S, Keum DH, Cho S, Perello D, Kim Y, Lee YH. Room Temperature Semiconductor-Metal Transition of MoTe₂ Thin Films Engineered by Strain. *Nano Lett*, 2016, 16: 188-193
- 77 Zhou L, Xu K, Zubair A, Liao AD, Fang W, Ouyang F, Lee Y-H, Ueno K, Saito R, Palacios T, Kong J, Dresselhaus MS. Large-Area Synthesis of High-Quality Uniform Few-Layer MoTe₂. *J Am Chem Soc*, 2015, 137: 11892-11895
- 78 Guo Y, Sun D, Ouyang B, Raja A, Song J, Heinz TF, Brus LE. Probing the Dynamics of the Metallic-to-Semiconducting Structural Phase Transformation in MoS₂ Crystals. *Nano Lett*, 2015, 15: 5081-5088
- 79 Dines MB. Intercalation in layered compounds. *J Chem Educ*, 1974, 51: 221-223
- 80 Dines MB. Lithium intercalation via n-butyllithium of the layered transition metal dichalcogenides. *Mater Res Bull*, 1975, 10: 287-291
- 81 Somoano RB, Hadek V, Rembaum A. Alkali metal intercalates of molybdenum disulfide. *J Chem Phys*, 1973, 58: 697-701
- 82 Whittingham MS. Lithium Batteries and Cathode Materials. *Chem Rev*, 2004, 104: 4271-4302
- 83 Eda G, Fujita T, Yamaguchi H, Voiry D, Chen M, Chhowalla M. Coherent Atomic and Electronic Heterostructures of Single-Layer MoS₂. *ACS Nano*, 2012, 6: 7311-7317

- 84 Chrissafis K, Zamani M, Kambas K, Stoemenos J, Economou NA, Samaras I, Julien C. Structural studies of MoS₂ intercalated by lithium. *Mater Sci Eng B*, 1989, 3: 145-151
- 85 Sandoval SJ, Yang D, Frindt R, Irwin J. Raman study and lattice dynamics of single molecular layers of MoS₂. *Phys Rev B*, 1991, 44: 3955-3962
- 86 Yang D, Sandoval SJ, Divigalpitaya W, Irwin J, Frindt R. Structure of single-molecular-layer MoS₂. *Phys Rev B*, 1991, 43: 12053-12056
- 87 Young VG, Mckelvy MJ, Glaunsinger WS, Von Dreele RB. Structural investigation of lithium-ammonia intercalation compounds of titanium sulfide (TiS₂). *Chem Mater*, 1990, 2: 75-81
- 88 Enyashin AN, Yadgarov L, Houben L, Popov I, Weidenbach M, Tenne R, Bar-Sadan M, Seifert G. New Route for Stabilization of 1T-WS₂ and MoS₂ Phases. *J Phys Chem C*, 2011, 115: 24586-24591
- 89 Rocquefelte X, Boucher F, Gressier P, Ouvrard G, Blaha P, Schwarz K. Mo cluster formation in the intercalation compound LiMoS₂. *Phys Rev B*, 2000, 62: 2397-2400
- 90 Kan M, Wang JY, Li XW, Zhang SH, Li YW, Kawazoe Y, Sun Q, Jena P. Structures and Phase Transition of a MoS₂ Monolayer. *J Phys Chem C*, 2014, 118: 1515-1522
- 91 Gao G, Jiao Y, Ma F, Jiao Y, Waclawik E, Du A. Charge Mediated Semiconducting-to-Metallic Phase Transition in Molybdenum Disulfide Monolayer and Hydrogen Evolution Reaction in New 1T' Phase. *J Phys Chem C*, 2015, 119: 13124-13128
- 92 Heising J, Kanatzidis MG. Structure of Restacked MoS₂ and WS₂ Elucidated by Electron Crystallography. *J Am Chem Soc*, 1999, 121: 638-643
- 93 Cheng Y, Nie A, Zhang Q, Gan L-Y, Shahbazian-Yassar R, Schwingschlogl U. Origin of the Phase Transition in Lithiated Molybdenum Disulfide. *ACS Nano*, 2014, 8: 11447-11453
- 94 Wang L, Xu Z, Wang W, Bai X. Atomic Mechanism of Dynamic Electrochemical Lithiation Processes of MoS₂ Nanosheets. *J Am Chem Soc*, 2014, 136: 6693-6697
- 95 Luo H, Xie W, Tao J, Inoue H, Gyenis A, Krizan JW, Yazdani A, Zhu Y, Cava RJ. Polytypism, polymorphism, and superconductivity in TaSe_{2-x}Te_x. *Proc Natl Acad Sci*, 2015, 112: E1174-E1180
- 96 Npwnpny RJJ. Polytypism in molybdenite (I): a non-equilibrium impurity-induced phenomenon. *Am Mineral*, 1974, 64: 758-767
- 97 Johari P, Shenoy VB. Tuning the Electronic Properties of Semiconducting Transition Metal Dichalcogenides by Applying Mechanical Strains. *ACS Nano*, 2012, 6: 5449-5456
- 98 Mitchell RS, Fujiki Y, Ishizawa Y. Structural polytypism of SnS₂. *Nature*, 1974, 247: 537-538
- 99 Palosz B, Steurer W, Schulz H. Refinement of SnS₂ polytypes 2H, 4H and 18R. *Acta Crystallogr Sect B*, 1990, 46: 449-455
- 100 Zhou X, Zhang Q, Gan L, Li H, Zhai T. Large-Size Growth of Ultrathin SnS₂ Nanosheets and High Performance for Phototransistors. *Adv Funct Mater*, 2016, 26: 4405-4413
- 101 Bilousov OV, Ren Y, Tömdahl T, Donzel-Gargand O, Ericson T, Platzer-Björkman C, Edoff M, Hägglund C. Atomic Layer Deposition of Cubic and Orthorhombic Phase Tin Monosulfide. *Chem Mater*, 2017, 29: 2969-2978
- 102 Zhou X, Gan L, Tian W, Zhang Q, Jin S, Li H, Bando Y, Golberg D, Zhai T. Ultrathin SnS₂ Flakes Grown by Chemical Vapor Deposition for High - Performance Photodetectors. *Adv Mater*, 2015, 27: 8035-8041
- 103 Ramakrishna Reddy KT, Koteswara Reddy N, Miles RW. Photovoltaic properties of SnS based solar cells. *Sol Energy Mater Sol Cells*, 2006, 90: 3041-3046
- 104 Sinsermsuksakul P, Sun L, Lee Sang W, Park Helen H, Kim Sang B, Yang C, Gordon Roy G. Overcoming Efficiency Limitations of SnS-Based Solar Cells. *Adv Energy Mater*, 2014, 4: 1400496-1400502
- 105 Xia J, Li X-Z, Huang X, Mao N, Zhu D-D, Wang L, Xu H, Meng X-M. Physical vapor deposition synthesis of two-dimensional orthorhombic SnS flakes with strong angle/temperature-dependent Raman responses. *Nanoscale*, 2016, 8: 2063-2070
- 106 Tian Z, Guo C, Zhao M, Li R, Xue J. Two-Dimensional SnS: A Phosphorene Analogue with Strong In-Plane Electronic Anisotropy. *ACS Nano*, 2017, 11: 2219-2226
- 107 Patel M, Chavda A, Mukhopadhyay I, Kim J, Ray A. Nanostructured SnS with inherent anisotropic optical properties for high photoactivity. *Nanoscale*, 2016, 8: 2293-2303
- 108 Su G, Hadjiev VG, Loya PE, Zhang J, Lei S, Maharjan S, Dong P, M. Ajayan P, Lou J, Peng H. Chemical Vapor Deposition of Thin Crystals of Layered Semiconductor SnS₂ for Fast Photodetection Application. *Nano Lett*, 2015, 15: 506-513
- 109 Hu Y, Luo B, Ye D, Zhu X, Lyu M, Wang L. An Innovative Freeze - Dried Reduced Graphene Oxide Supported SnS₂ Cathode Active Material for Aluminum - Ion Batteries. *Adv Mater*, 2017, 29: 1606132-1606137
- 110 Qu B, Ma C, Ji G, Xu C, Xu J, Meng Ying S, Wang T, Lee Jim Y. Layered SnS₂-Reduced Graphene Oxide Composite: A High-Capacity, High-Rate, and Long-Cycle Life Sodium - Ion Battery Anode Material. *Adv Mater*, 2014, 26: 3854-3859
- 111 Ye G, Gong Y, Lei S, He Y, Li B, Zhang X, Jin Z, Dong L, Lou J, Vajtai R, Zhou W, Ajayan PM. Synthesis of large-scale atomic-layer SnS₂ through chemical vapor deposition. *Nano Res*, 2017, 10: 2386-2394
- 112 Brent JR, Lewis DJ, Lorenz T, Lewis EA, Savjani N, Haigh SJ, Seifert G, Derby B, O'brien P. Tin(II) Sulfide (SnS) Nanosheets by Liquid-Phase Exfoliation of Herzenbergite: IV-VI Main Group Two-Dimensional Atomic Crystals. *J Am Chem Soc*, 2015, 137: 12689-12696
- 113 Fernandes PA, Sousa MG, Salome PMP, Leitao JP, Da Cunha AF. Thermodynamic pathway for the formation of SnSe and SnSe₂ polycrystalline thin films by selenization of metal precursors. *CrystEngComm*, 2013, 15: 10278-10286
- 114 Huang Y, Xu K, Wang Z, Shifa TA, Wang Q, Wang F, Jiang C, He J. Designing the shape evolution of SnSe₂ nanosheets and their optoelectronic properties. *Nanoscale*, 2015, 7: 17375-17380
- 115 Zhou T, Pang WK, Zhang C, Yang J, Chen Z, Liu HK, Guo Z. Enhanced Sodium-Ion Battery Performance by Structural Phase Transition from Two-Dimensional Hexagonal-SnS₂ to Orthorhombic-SnS. *ACS Nano*, 2014, 8: 8323-8333
- 116 Sutter E, Huang Y, Komsa HP, Ghorbani-Asl M, Krashennikov AV, Sutter P. Electron-Beam Induced Transformations of Layered Tin Dichalcogenides. *Nano Lett*, 2016, 16: 4410-4416
- 117 Mitchell RS, Fujiki Y, Ishizawa Y. Structural polytypism of tin disulfide: Its relationship to environments of formation. *J Cryst Growth*, 1982, 57: 273-279
- 118 Von Schnering HG, Wiedemeier H. The high temperature structure of β-SnS and β-SnSe and the B16-to-B33 type λ-transition path. *Z Kristallogr*, 1981, 156: 143-150
- 119 Chattopadhyay T, Pannetier J, Von Schnering HG. Neutron diffraction study of the structural phase transition in SnS and SnSe. *J Phys Chem Sol*, 1986, 47: 879-885
- 120 Bletskan DI. Phase Equilibrium in binary A^{IV}B^{VI} Part. III Systems Sn-chalcogenides. *J Ovonic Res*, 2005, 61-69
- 121 Tian Z, Zhao M, Xue X, Xia W, Guo C, Guo Y, Feng Y, Xue J. Lateral Heterostructures Formed by Thermally Converting n-Type SnSe₂ to p-Type SnSe. *ACS Appl Mater Interfaces*, 2018, 10: 12831-12838
- 122 Sharma RC, Chang YA. The Se-Sn (Selenium-Tin) system. *Bull Alloy Phase Diagrams*, 1986, 7: 68-72
- 123 Jain PK, Huang X, El-Sayed IH, El-Sayed MA. Noble Metals on the Nanoscale: Optical and Photothermal Properties and Some Applications in Imaging, Sensing, Biology, and Medicine. *Acc Chem Res*, 2008, 41: 1578-1586
- 124 Qin HL, Wang D, Huang ZL, Wu DM, Zeng ZC, Ren B, Xu K, Jin J. Thickness-Controlled Synthesis of Ultrathin Au Sheets and Surface Plasmonic Property. *J Am Chem Soc*, 2013, 135: 12544-12547
- 125 Saleem F, Zhang Z, Xu B, Xu X, He P, Wang X. Ultrathin Pt-Cu Nanosheets and Nanocones. *J Am Chem Soc*, 2013, 135: 18304-18307
- 126 Fan Z, Huang X, Tan C, Zhang H. Thin metal nanostructures: synthesis, properties and applications. *Chem Sci*, 2015, 6: 95-111
- 127 Li Q, Wu L, Wu G, Su D, Lv H, Zhang S, Zhu W, Casimir A, Zhu H, Mendoza-Garcia A, Sun S. New Approach to Fully Ordered fct-FePt Nanoparticles for Much Enhanced Electrocatalysis in Acid. *Nano Lett*, 2015, 15: 2468-2473
- 128 Liu X, Luo J, Zhu J. Size Effect on the Crystal Structure of Silver Nanowires. *Nano Lett*, 2006, 6: 408-412
- 129 Eustis S, El-Sayed MA. Why gold nanoparticles are more precious than pretty gold: Noble metal surface plasmon resonance and its enhancement of the radiative and nonradiative properties of nanocrystals of different shapes. *Chem Soc Rev*, 2006, 35: 209-217
- 130 Xia Y, Xiong Y, Lim B, Skrabalak SE. Shape-Controlled Synthesis of Metal Nanocrystals: Simple Chemistry Meets Complex Physics? *Angew Chem Int Ed*, 2009, 48: 60-103
- 131 Huang B, Kobayashi H, Yamamoto T, Matsumura S, Nishida Y, Sato

- K, Nagaoka K, Kawaguchi S, Kubota Y, Kitagawa H. Solid-Solution Alloying of Immiscible Ru and Cu with Enhanced CO Oxidation Activity. *J Am Chem Soc*, 2017, 139: 4643-4646
- 132 Zhang Q, Kusada K, Wu D, Yamamoto T, Toriyama T, Matsumura S, Kawaguchi S, Kubota Y, Kitagawa H. Selective control of fcc and hcp crystal structures in Au–Ru solid-solution alloy nanoparticles. *Nat Commun*, 2018, 9: 510-518
- 133 Indrani C, Sharmila NS, Smita G, Umesh VW, Pushan A. A stable, quasi-2D modification of silver: optical, electronic, vibrational and mechanical properties, and first principles calculations. *J Phys: Condens Matter*, 2014, 26: 025402-025411
- 134 Kusada K, Kobayashi H, Yamamoto T, Matsumura S, Sumi N, Sato K, Nagaoka K, Kubota Y, Kitagawa H. Discovery of Face-Centered-Cubic Ruthenium Nanoparticles: Facile Size-Controlled Synthesis Using the Chemical Reduction Method. *J Am Chem Soc*, 2013, 135: 5493-5496
- 135 Huang X, Li H, Li SZ, Wu SX, Boey F, Ma J, Zhang H. Synthesis of Gold Square-like Plates from Ultrathin Gold Square Sheets: The Evolution of Structure Phase and Shape. *Angew Chem Int Ed*, 2011, 50: 12245-12248
- 136 Liao H, Zhu J, Hou Y. Synthesis and electrocatalytic properties of PtBi nanoplatelets and PdBi nanowires. *Nanoscale*, 2014, 6: 1049-1055
- 137 Fan Z, Zhu Y, Huang X, Han Y, Wang Q, Liu Q, Huang Y, Gan CL, Zhang H. Synthesis of Ultrathin Face-Centered-Cubic Au@Pt and Au@Pd Core-Shell Nanoplates from Hexagonal-Close-Packed Au Square Sheets. *Angew Chem Int Ed*, 2015, 54: 5672-5676
- 138 Fan Z, Chen Y, Zhu Y, Wang J, Li B, Zong Y, Han Y, Zhang H. Epitaxial growth of unusual 4H hexagonal Ir, Rh, Os, Ru and Cu nanostructures on 4H Au nanoribbons. *Chem Sci*, 2017, 8: 795-799
- 139 Guo Q, Zhao Y, Mao WL, Wang Z, Xiong Y, Xia Y. Cubic to Tetragonal Phase Transformation in Cold-Compressed Pd Nanocubes. *Nano Lett*, 2008, 8: 972-975
- 140 Diao J, Gall K, Dunn ML. Surface-stress-induced phase transformation in metal nanowires. *Nat Mater*, 2003, 2: 656-660
- 141 Kondo Y, Takayanagi K. Synthesis and Characterization of Helical Multi-Shell Gold Nanowires. *Science*, 2000, 289: 606-609
- 142 Chakraborty I, Carvalho D, Shirodkar SN, Lahiri S, Bhattacharyya S, Banerjee R, Waghmare U, Ayyub P. Novel hexagonal polytypes of silver: growth, characterization and first-principles calculations. *J Phys: Condens Matter*, 2011, 23: 325401-325412
- 143 Gao K, Wang Y, Wang Z, Zhu Z, Wang J, Luo Z, Zhang C, Huang X, Zhang H, Huang W. Ru nanodendrites composed of ultrathin fcc/hcp nanoblades for the hydrogen evolution reaction in alkaline solutions. *Chem Commun*, 2018, 54: 4613-4616
- 144 Kitchin JR, Nørskov JK, Barteau MA, Chen JG. Role of Strain and Ligand Effects in the Modification of the Electronic and Chemical Properties of Bimetallic Surfaces. *Phys Rev Lett*, 2004, 93: 156801-156804
- 145 Titmuss S, Wander A, King DA. Reconstruction of Clean and Adsorbate-Covered Metal Surfaces. *Chem Rev*, 1996, 96: 1291-1306
- 146 Vericat C, Vela ME, Benitez G, Carro P, Salvarezza RC. Self-assembled monolayers of thiols and dithiols on gold: new challenges for a well-known system. *Chem Soc Rev*, 2010, 39: 1805-1834
- 147 Ghosh Chaudhuri R, Paria S. Core/Shell Nanoparticles: Classes, Properties, Synthesis Mechanisms, Characterization, and Applications. *Chem Rev*, 2012, 112: 2373-2433
- 148 Jiang H-L, Akita T, Ishida T, Haruta M, Xu Q. Synergistic Catalysis of Au@Ag Core-Shell Nanoparticles Stabilized on Metal–Organic Framework. *J Am Chem Soc*, 2011, 133: 1304-1306
- 149 Wang D, Xin HL, Hovden R, Wang H, Yu Y, Muller DA, Disalvo FJ, Abruna HD. Structurally ordered intermetallic platinum–cobalt core–shell nanoparticles with enhanced activity and stability as oxygen reduction electrocatalysts. *Nat Mater*, 2012, 12: 81-87
- 150 Kim Y-H, Jun Y-w, Jun B-H, Lee S-M, Cheon J. Sterically Induced Shape and Crystalline Phase Control of GaP Nanocrystals. *J Am Chem Soc*, 2002, 124: 13656-13657
- 151 Liu Y, Wang C, Wei Y, Zhu L, Li D, Jiang JS, Markovic NM, Stamenkovic VR, Sun S. Surfactant-Induced Postsynthetic Modulation of Pd Nanoparticle Crystallinity. *Nano Lett*, 2011, 11: 1614-1617
- 152 Huang X, Li SZ, Wu SX, Huang YZ, Boey F, Gan CL, Zhang H. Graphene Oxide-Templated Synthesis of Ultrathin or Tadpole-Shaped Au Nanowires with Alternating hcp and fcc Domains. *Adv Mater*, 2012, 24: 979-983
- 153 Rajaji V, Dutta U, Sreeparvathy PC, Sarma SC, Sorb YA, Joseph B, Sahoo S, Peter SC, Kanchana V, Narayana C. Structural, vibrational, and electrical properties of 1T TiTe₂ under hydrostatic pressure: Experiments and theory. *Phys Rev B*, 2018, 97: 085107-085107
- 154 Besson JM, Itié JP, Polian A, Weill G, Mansot JL, Gonzalez J. High-pressure phase transition and phase diagram of gallium arsenide. *Phys Rev B*, 1991, 44: 4214-4234
- 155 Qi Y, Shi W, Naumov Pavel G, Kumar N, Sankar R, Schnelle W, Shekhar C, Chou FC, Felser C, Yan B, Medvedev Sergey A. Topological Quantum Phase Transition and Superconductivity Induced by Pressure in the Bismuth Tellurohalide BiTeI. *Adv Mater*, 2017, 29: 1605965-1605971
- 156 Tran MK, Levallois J, Lerch P, Teyssier J, Kuzmenko AB, Autès G, Yazeyev OV, Ubal dini A, Giannini E, Van Der Marel D, Akrap A. Infrared- and Raman-Spectroscopy Measurements of a Transition in the Crystal Structure and a Closing of the Energy Gap of BiTeI under Pressure. *Phys Rev Lett*, 2014, 112: 47402-47406
- 157 Mao HK, Bell PM, Shaner JW, Steinberg DJ. Specific volume measurements of Cu, Mo, Pd and Ag and calibration of ruby R1 fluorescence pressure gauge from 0.06 to 1Mbar. *J Appl Phys*, 1978, 49: 3276-3283
- 158 McMahon MI, Nelmel RJ. High-pressure structures and phase transformations in elemental metals. *Chem Soc Rev*, 2006, 35: 943-963
- 159 Koski KJ, Kamp NM, Smith RK, Kunz M, Knight JK, Alivisatos AP. Structural distortions in 5-10 nm silver nanoparticles under high pressure. *Phys Rev B*, 2008, 78: 165410-165419
- 160 Tong C-J, Zhang H, Zhang Y-N, Liu H, Liu L-M. New manifold two-dimensional single-layer structures of zinc-blende compounds. *J Mater Chem A*, 2014, 2: 17971-17978
- 161 Singh AK, Zhuang HL, Hennig RG. Ab initio synthesis of single-layer III-V materials. *Phys Rev B*, 2014, 89: 245431-245440
- 162 Fan Z, Zhang H. Template Synthesis of Noble Metal Nanocrystals with Unusual Crystal Structures and Their Catalytic Applications. *Acc Chem Res*, 2016, 49: 2841-2850
- 163 Fan Z, Huang X, Chen Y, Huang W, Zhang H. Facile synthesis of gold nanomaterials with unusual crystal structures. *Nat Protoc*, 2017, 12: 2367-2378
- 164 Lu Q, Wang A-L, Gong Y, Hao W, Cheng H, Chen J, Li B, Yang N, Niu W, Wang J, Yu Y, Zhang X, Chen Y, Fan Z, Wu X-J, Chen J, Luo J, Li S, Gu L, Zhang H. Crystal phase-based epitaxial growth of hybrid noble metal nanostructures on 4H/fcc Au nanowires. *Nat Chem*, 2018, 10: 456-461
- 165 Tan C, Chen J, Wu X-J, Zhang H. Epitaxial growth of hybrid nanostructures. *Nat Rev Mater*, 2018, 3: 17089-17101

二维材料的晶相调控

王加亮¹、韦扬¹、李海^{1*}、黄晓^{1*}、张华^{2*}

1 南京工业大学, 先进材料研究院

2 新加坡南洋理工大学, 材料科学与工程学院

摘要

多晶型是指一种化合物在固态时存在两种及以上的晶体排列方式, 是晶体独有的特征。近来科学家在对二维材料的广泛研究和深入探索的基础上, 发现了许多新的晶体结构。不同于室温条件下的块状材料, 这些材料在二维尺度上展现出晶相相关的全新性质。本文综述了 VI 族过渡金属硫化物、第 IV 主族金属硫化物以及贵金属等二维材料在晶相控制方面的最新进展。首先简要介绍了每类材料可能存在的晶相结构及其性质, 然后详细讨论了影响晶体结构的因素, 进而提出相应的晶相控制策略。最后描述了该研究方向在未来可能遇到的机遇与挑战。

关键词: 晶相控制, 金属硫族化合物, 贵金属, 二维材料